Dynamic Modeling of Blown-Film Extrusion

J. CARL PIRKLE, JR., *and* RICHARD D. BRAATZ

600 South Mathews Avenue, Box C-3
University of Illinois at Urbana-Champaign
Urbana, Illinois 61801

Past dynamic studies of blown-film extrusion have been confined to the stability analysis of the linearized equations. The full set of nonlinear equations comprises a system of partial differential and algebraic equations with boundary conditions that vary from author to author. In this paper, the Numerical-Method-of-Lines, which combines finite-difference methods with ordinary differential/algebraic equation integrators, is used to solve the full system. Appropriate boundary conditions are selected to give physical results that compare well with experiment. An important boundary condition is the "minimum order reduction" condition on the gradient of the bubble-tube radius with respect to distance above the extrusion die (the axial position). Transient startups and operational disturbances are examined. Calculations show the influence of oscillations in operating conditions such as heat transfer or inflation pressure on the bubble-tube radius and film thickness. Steady-state results obtained by integrating the transient equations for a sufficiently long time are qualitatively in agreement with experiment, in contrast to past simulations of these equations.

INTRODUCTION

Blown film extrusion is used to manufacture plastic bags and sheets of thin thermoplastic films (1). Although significant effort has been made in the steady-state analysis of blown film extrusion, little has been attempted other than linearized stability analysis for the dynamic modeling of this process. Dynamic modeling enables the examination of strategies for process startup, for handling process upsets, and for process control.

Here the system of PDEs for the dynamic modeling of blown film extrusion is solved using Numerical-Method-of-Lines (NMOL) (2). The dynamic and steady-state solutions are presented for the Pearson-Petrie model (3, 4), which has been a mainstay for modeling blown film extrusion of thin films. The NMOL method (spatial discretization of variables and approximation of derivatives by finite differences, followed by time integration to steady-state) avoids the instability of shooting methods used to solve steady-state equations directly. We show that the NMOL method yields steady-state results that are qualitatively different from the simulation results reported for the Pearson-Petrie model by Liu *et al.* (5). Furthermore, our results are in good qualitative agreement with the experimental results (6). This finding is important, because the steady-state simulation results obtained by Liu caused him to advocate an alternative model, the quasi-cylindrical model, to the thin shell model of Pearson and Petrie. This quasi-cylindrical model was used by subsequent researchers (7).

This paper describes the blown film extrusion process, presents the dynamic equations for Pearson-Petrie model, discusses some steady-state results (obtained from the dynamic model at long times), and examines the dynamic response of the model to both startup and various process disturbances.

DESCRIPTION OF THE BLOWN FILM EXTRUSION PROCESS

Molten polymer is extruded through an annular die while air is fed through an inner concentric bubble-tube (see *Fig. 1*). This internal air causes the cylindrical film to inflate, increasing the radius of the polymer bubble by stretching it, and decreasing the film thickness. Simultaneously, the guide rolls above the die flatten the film and the nip rolls subject the film to tension in the axial (upward from the die) direction. External air supplied from a concentric outer ring cools the film. The resulting temperature reduction increases the viscosity of the rising film and eventually induces crystallization as the temperature drops below the melting point of the polymer. The crystallization, in turn, causes an additional increase in viscosity, and the polymer solidifies.

The solidification zone is called the freeze zone or frost zone (1). Within this region, the rapidly increasing viscous stiffness causes the bubble radius and the film thickness to stabilize, changing very little as the film heads upward toward the nip rolls. The nip rolls and the bubble inflation create an elongating force on the polymer bubble-tube. Also, the inflating air causes

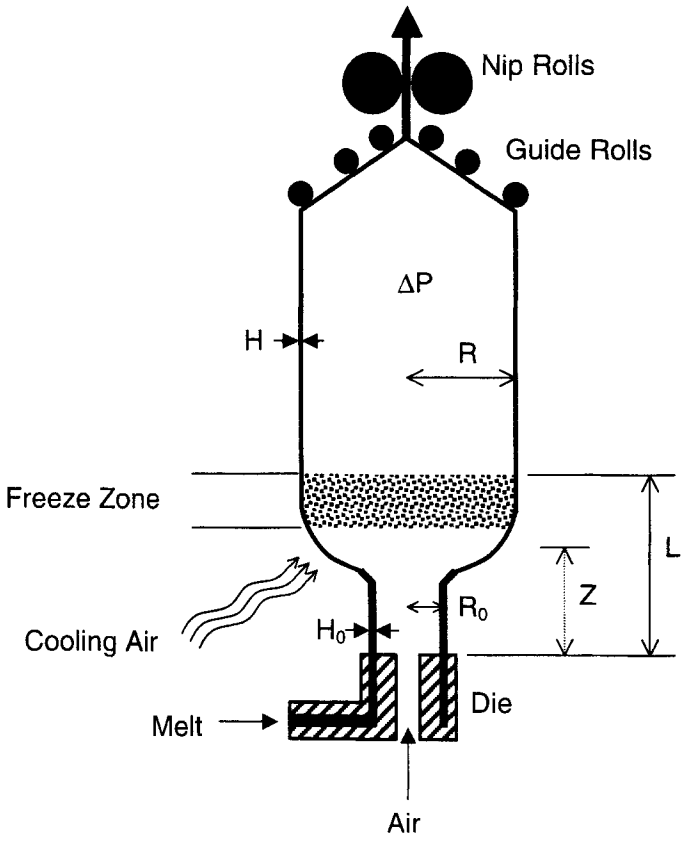

Fig. 1. Schematic of blown film extrusion.

a circumferential tension on the bubble-tube. The resulting biaxial stress can further induce crystallization, an action termed flow-induced crystallization. Although this effect has been included in a recent paper (7), it is neglected in most models of blown film extrusion (8, 9, 10).

Pearson and Petrie and others have developed steady-state models to describe the blown film extrusion process in the limit of very thin films (11, 12). In these models, variations of the physical variables across the thin film are neglected, leaving the variables as functions of axial position (height above the die) only. Generally, these models involve the continuity equations, momentum equations in the axial and circumferential directions, and some type of constitutive relation. In later applications, these were coupled with equations for energy and crystallization kinetics in order to follow the effect of temperature and crystallization on the viscosity (5, 13).

PREVIOUS DYNAMIC MODELS

The time-dependent equations for the thin film model of blown film extrusion have been presented by various authors (8, 10, 14). The equations were linearized in order to perform stability analysis, but solutions for the original nonlinear equations were not presented. Owing to differences in numerical methods and constitutive relations, there is some disagreement in the results reported by these investigators.

Yeow (14) presented the unsteady-state extension of the Pearson-Petrie model for blown-film extrusion. He derived the dynamic deformation rate tensor for the moving film and performed a stability analysis on the linearized version of the dynamic equations. Cain and Denn (8) followed up this work using a finite difference method and found qualitatively and quantatively different results. Yoon and Park (10) rederived the dynamic equations and performed another linearized stability analysis.

In this paper, we solve the dynamic continuity and momentum equations by the numerical method of lines (2). These equations are augmented with the dynamic energy balance equations and the constitutive relation used by Liu *et al.* (5), which allows reduction in viscosity by stress-induced deformation thinning as well as an increase in viscosity by temperature reduction and crystallization.

DYNAMIC PEARSON-PETRIE MODEL

Like the steady-state Pearson-Petrie model, the dynamic model of film motion neglects inertial terms, surface tension, drag effects of the cooling air, and gravity. Dimensionless variables are used in the equations that follow. The dimensional and dimensionless variables are defined in *Tables 1* and *2*, respectively. The axial position variable Z is bounded by $Z = 0$ at the die and $Z = L$ at the upper boundary of the frost zone, which is called the frost line. The frost zone begins at the onset

Table 1. Symbols for Variables and Constants: Dimensional.

b	Exponent for denominator term of viscosity factor
C_{pf}	Specific heat of polymer
C_3	Coefficient in crystallization rate expression
H_0	Film thickness as it exits the die at Z = 0
H	Film thickness at axial position Z
H_L	Film thickness at top boundary of freeze zone
k_{crys}	Crystallization rate coefficient
L	Axial position corresponding to top boundary of freeze zone
N_Z	Number of grid points in discretization of axial coordinate
R	Radius of film bubble tube at axial position Z
R_L	Final radius of film bubble tube at top boundary of freeze zone
R_0	Radius of film bubble tube as it exits the die at Z = 0
t	Time
T	Temperature of film bubble tube at position Z
T_{air}	Temperature of cooling air
T_∞	Equal to T_g − 30 K, where T_g is the polymer glass transition temperature
T_m	Melt temperature of polymer
T_0	Temperature of film bubble tube as it exits die at Z = 0
U^*	Activation energy for segmental jump rate in polymers
V	Velocity of film at axial position Z
V_L	Velocity of film at top boundary of freeze zone
V_0	Velocity of film as it exits the die at Z = 0
Z	Axial position measured upward from position of die
α_1	Adjustment coefficient for viscosity factor
α_2	Adjustment coefficient for crystallization term in viscosity factor
β_1	Adjustment coefficient for temperature dependence of viscosity factor
β_2	Exponent for crystallization dependence of viscosity factor
X	Local fraction of crystallinity
X_f	Final crystallinity
ΔH_{crys}	Heat of crystallization
ΔP	Inflation pressure, relative to ambient pressure
λ	Relaxation time
Π_d	Second invariant of the deformation rate tensor
ρ	Polymer density
$\Re$	Universal gas constant
μ	Viscosity of polymer
μ_0	Viscosity of polymer as it exits die

of crystallization and ends where further changes in bubble-tube dimensions are imperceptible because of the extremely large viscosity. In simulations L is taken to be sufficiently large that the bubble tube is in this frozen state at Z = L.

In the Pearson-Petrie thin shell model, the dynamic continuity equation takes the dimensionless form (10):

$$\psi\left(h\frac{\partial r}{\partial \tau}+r\frac{\partial h}{\partial \tau}\right)+\frac{rhy}{\psi}\frac{\partial y}{\partial \tau}+rh\frac{\partial v}{\partial \varsigma}+rv\frac{\partial h}{\partial \varsigma}+hvy=0 \tag{1}$$

where $\psi=\sqrt{1+(\partial r/\partial \varsigma)^2}$. The dynamic momentum equation in the axial direction is:

$$-\frac{r}{\psi}\frac{\partial h}{\partial \tau}+\frac{rhy}{\psi^3}\frac{\partial y}{\partial \tau}+\frac{rh}{\psi^2}\frac{\partial v}{\partial \varsigma}-\frac{rv}{\psi^2}\frac{\partial h}{\partial \varsigma}=\frac{F_m+B(r^2-r_f^2)}{2\eta} \tag{2}$$

where

$$y=\frac{\partial r}{\partial \varsigma}, \tag{3}$$

F_m is the dimensionless machine tension, B is the dimensionless inflation pressure defined in *Table 2*, and r_f is the value of the dimensionless bubble radius r at $\varsigma = L/R_0$ and time τ. For the purpose of computing steady-state results and subsequent interpretation, the modified tension $F = F_m - Br_f^2$ is used in this paper. The modified tension F is especially useful as a continuation parameter in getting around turning points when generating blowup ratio versus thickness reduction plots.

The dynamic momentum equation in the circumferential direction is:

$$\psi\frac{h}{r^2}\frac{\partial r}{\partial \tau}+\left(\frac{1}{\psi}\frac{\partial y}{\partial \varsigma}-\frac{\psi}{r}\right)\frac{\partial h}{\partial \tau}-\frac{hy}{\psi^3}\frac{\partial y}{\partial \varsigma}\frac{\partial y}{\partial \tau}-\frac{1}{\psi^2}\frac{\partial y}{\partial \varsigma}\left(h\frac{\partial v}{\partial \varsigma}-v\frac{\partial h}{\partial \varsigma}\right)+\frac{v}{r^2}\left(hy-r\frac{\partial h}{\partial \varsigma}\right)=\frac{B}{\eta}\psi^2 \tag{4}$$

The boundary conditions for the Pearson-Petrie model have been the subject of some discussion. At the die, the three boundary conditions for bubble-tube radius, film thickness, and film velocity are

$$r=1 \text{ at } \varsigma=0, \tag{5}$$

Table 2. Symbols for Variables and Constants: Dimensionless.

B	Dimensionless pressure force = $\Delta P R_0^2/[2 \mu_0 H_0 V_0]$
F	Modified tension
F_m	Dimensionless machine tension
h	Dimensionless film thickness = H/H_0
r	Dimensionless film bubble-tube radius = R/R_0
r_L	Dimensionless film bubble-tube radius at top boundary of freeze zone
x	Dimensionless crystallinity = X/X_f
v	Dimensionless film velocity = V/V_0
v_L	Take-up ratio = V_L/V_0
y	Dimensionless derivative of radius with respect to axial position = $\partial r/\partial \varsigma$
ς	Dimensionless axial position = Z/R_0
η	Dimensionless viscosity factor = μ/μ_0
θ	Dimensionless temperature = T/T_0
θ_{air}	Dimensionless temperature of air = T_{air}/T_0
ν	Dimensionless frequency of oscillation, cycles per dimensionless time unit
τ	Dimensionless time = $t V_0/R_0$
ψ	Dimensionless curvature

$$h = 1 \text{ at } \varsigma = 0, \tag{6}$$

$$v = 1 \text{ at } \varsigma = 0, \tag{7}$$

respectively.

For the axial gradient of the bubble-tube radius, the suggested boundary conditions are

$$y = y_0 \text{ at } \varsigma = 0 \tag{8a}$$

or

$$y = 0 \text{ at } \varsigma = L/R_0 \tag{8b}$$

or

$$\psi \frac{h}{r^2}\frac{\partial r}{\partial \tau} + \left(-\frac{\psi}{r}\right)\frac{\partial h}{\partial \tau} + \frac{v}{r^2}\left(hy - r\frac{\partial h}{\partial \varsigma}\right) = \frac{B}{\eta}\psi^2 \text{ at } \varsigma = L/R_0 \tag{8c}$$

The first choice corresponds to the emergence of the molten polymer from the die at some preset angle to the vertical direction (e.g., $y_0 = 0$ for perfectly parallel flow). The difficulty with the first boundary condition is the tendency for the melt leaving the die to expand or contract instantly. The second boundary condition is equivalent to cessation of the bubble-tube expansion at the top boundary of the frost zone Z = L. The problem with this boundary condition is the tendency for the gradient of the bubble-tube radius to become exceedingly small anyway because of the stiffening of the polymer, and the imposition of *Eq 8b* creates a nonphysical kink at $\varsigma = L/R_0$. The last boundary condition (*Eq 8c*) results from setting $\partial y/\partial \varsigma$ to zero in *Eq 4*. This type of boundary condition has been discussed and implemented by Schiesser (2) in the context of general convection-diffusion equations, in which extensive literature has been written on the selection of outflow boundary conditions (15). We show later that *Eq 8c* is the preferred boundary condition at $\varsigma = L/R_0$.

The energy balance and crystallization equations are

$$\frac{\partial \theta}{\partial \tau} + v\frac{\partial \theta}{\partial \varsigma} + B_2\frac{(\theta - \theta_{air})}{h} - B_3 B_4 F_\theta (1 - x) = 0 \tag{9}$$

$$\frac{\partial x}{\partial \tau} + v\frac{\partial x}{\partial \varsigma} - B_4 F_\theta (1 - x) = 0 \tag{10}$$

where

$$B_2 = \frac{U_h R_0}{\rho C_{pf} H_0 V_0} \tag{11}$$

$$B_3 = \frac{\Delta H_{crys} X_f}{C_{pf} T_0} \tag{12}$$

$$B_4 = \frac{R_0 k_{crys}}{V_0} \tag{13}$$

Here, the heat-loss term takes the form of Newton's law of convective cooling. Heat loss due to radiation is about 20% of that due to convection, so the effect of radiation has been lumped into the convection term by increasing the heat transfer coefficient U_h. The function F_θ is the temperature-dependent factor for the rate of crystallization:

$$F_\theta = 0 \quad \text{for} \quad \theta \geq \theta_m \tag{14a}$$

$$F_\theta = \exp\left[-\frac{B_{F1}}{(\theta - \theta_c)} - \frac{B_{F2}}{\theta(\theta_m - \theta)}\right] \quad \text{for} \quad \theta < \theta_m \tag{14b}$$

where the dimensionless constants B_{F1}, B_{F2}, θ_m, and θ_c are

$$B_{F1} = \frac{U^*}{\Re T_0} \tag{15}$$

$$B_{F2} = \frac{C_3}{T_0^2} \tag{16}$$

$$\theta_m = \frac{T_m}{T_0} \tag{17}$$

$$\theta_c = \frac{T_\infty}{T_0} \tag{18}$$

Like previous studies of blown-film extrusion (an exception being Doufas and McHugh (7)), flow-induced crystallization is ignored.

The temperature and degree of crystallization are specified at the die

$$\theta = 1 \text{ at } \varsigma = 0 \tag{19}$$

$$x = 0 \text{ at } \varsigma = 0 \tag{20}$$

CONSTITUTIVE RELATION

A non-Newtonian constitutive relationship for describing the viscosity of the polymer during its extrusion, that takes deformation thinning into account, is (5)

$$\mu = \mu_0 \eta, \tag{21}$$

where the base viscosity μ_0 is

$$\mu_0 = \alpha_1 \exp\left(\frac{\beta_1}{T_0}\right). \tag{22}$$

and the dimensionless viscosity factor η, which accounts for temperature change and crystallization, is

$$\eta = \frac{\alpha_1 \exp\left(\frac{\beta_1}{T_0}\frac{1}{\theta}\right) \exp(\alpha_2 x^{\beta_2})}{1 + (\lambda\sqrt{\Pi_d})^b} \tag{23}$$

Here, α_1, α_2, β_1, β_2, and b are measured or adjusted constants, and Π_d and λ are the second invariant of the deformation rate tensor and the relaxation time, respectively. In terms of the dependent variables, the expression for Π_d is

$$\Pi_d = 2\left(\frac{V_0}{R_0}\right)^2 \left[\left(\frac{1}{r}\frac{\partial r}{\partial \varsigma}\right)^2 + \left(\frac{1}{h}\frac{\partial h}{\partial \varsigma}\right)^2 + \left(\frac{1}{r}\frac{\partial r}{\partial \varsigma}\right)\left(\frac{1}{h}\frac{\partial h}{\partial \varsigma}\right)\right] v^2 \tag{24}$$

Whenever $\lambda = 0$, *Eq 23* describes a Newtonian fluid.

Equation 23 was elected for the calculations reported here as it was the constitutive relation used by Liu *et al.* (5). This allows a direct comparison of results obtained with our numerical method and the inclusion of the exit boundary condition, *Eq 8c*, with those of Liu.

NUMERICAL METHOD OF SOLUTION

The above system of algebraic and partial differential equations is solved using the numerical method of lines (NMOL) (2). This involves discretizing the equations in the spatial variable ς at a number of grid points N_Z. Spatial derivatives such as $\partial v/\partial \varsigma$ are approximated as five-point finite differences in order to achieve 4th-order accuracy, thus eliminating the spatial variable as an independent variable. A variable-grid spacing technique that allows a choice of such 5-point finite differences is coded in the subroutine DSS032 (16). The spatial discretization converts *Eq 1, 2, 4, 8c, 9,* and *10* to a set of $(5N_Z + 1)$ coupled ordinary differential equations containing time derivatives for the values of r, h, y, θ, and x at each grid point. Upon discretization, *Eq 4* gives a set of N_Z algebraic equations (no time derivatives). The boundary conditions (*Eqs 5, 6, 7, 19,* and *20*) are included in the DAE system as algebraic equations.

The resulting system of ordinary differential and algebraic equations (DAEs) is solved using the double precision version of the solver DASSL (17, 18). All computations were performed in double precision Fortran using a 900 MHz Athlon processor-based computer. In coding the dynamic equations, the first grid point was selected at the beginning of the die ($Z = 0$). Then the discretized equations were written for each grid point before moving on to the next. This resulted in a banded Jacobian that greatly speeded up the calculations with DASSL.

The calculations started with 41 grid points, which were increased until the computed results were unchanged within a minimum of four significant figures of accuracy. The grid point allocation that met this criterion was 71 points uniformly distributed from ς = 0 to 0.4, and 30 points uniformly distributed from ς = 0.4 to 1.0. Spatial derivatives were approximated by using five-point biased upwind differences for $\partial r/\partial \varsigma$, $\partial h/\partial \varsigma$, $\partial v/\partial \varsigma$, $\partial \theta/\partial \varsigma$, and $\partial x/\partial \varsigma$ and using five-point centered differences for $\partial y/\partial \varsigma$ (which is equal to $\partial^2 r/\partial \varsigma^2$).

The startup condition used in the calculations consisted of extruding and attaching the bubble tube to the nip rolls under conditions of uniform (with respect to Z) bubble-tube radius and film thickness. The two stress constants B and F_m are then increased from zero to positive values by using the switching functions:

$$B(1 - \exp(-\tau^2/\tau_s^2)) \tag{25}$$

$$F_m(1 - \exp(-\tau^2/\tau_s^2)) \tag{26}$$

where τ_s is a switching time constant that can be set to be fast or slow, depending on the simulation. The switching function goes from zero to one as increases from zero.

The value of B is dependent on the pressure difference ΔP across the film, as shown in the definitions of *Table 1*. Whenever a given steady-state take-up ratio is desired, F_m (or F) is adjusted until the take-up velocity reaches the desired value. The adjustment of F_m (or F) is accomplished by regula falsi interpolative root finding (19).

SIMULATIONS OF PEARSON-PETRIE MODEL

Table 3 contains the operating conditions for the simulation and also gives the values for the physical parameters. The values of parameters associated with

Table 3. Values of Constants Used in Simulations.

λ	4.68 s
b	0.68
C_{pf}	2.43 kJ/kg-K
C_3	85,000 K^2
H_0	0.095 cm
k_{crys}	2670 s^{-1}
R_0	0.746 cm
T_{air}	331 K
T_g	118 K
T_m	414 K
T_0	463 K
U_h	50.27 W/m^2-K
U^*	6284 kJ/kmol
V_0	0.366 cm/s
α_1	0.96 Pa-s
α_2	13.5
β_1	4480 K
β_2	0.4
X_f	0.44
ΔH_{crys}	293.2 kJ/kg
ρ	919 kg/m^3
τ_s	1.0

the constitutive relation were obtained from the experimental work of Liu *et al.* (5, 6, 20, 21). They correspond to a low density polyethylene (LDPE) provided by Dow Chemical Company. The inflation pressure ΔP ranged from 0 to 270 Pa. The take-up ratio v_L, which is the film velocity at Z = L divided by the film velocity at Z = 0, varied from 2.988 to 5.200, and the temperature T_0 exiting the die varied from 443 to 467 K.

As most of the previous simulations for blown-film extrusion were at steady state, the steady-state results of our model are first compared with the results of other investigators. Here the dynamic computations are carried out for a long enough period of time that the steady state was reached (in our case τ = 5000 was used, which was more than sufficient). The "minimally reduced" outflow boundary condition *8c* was used as extensive computations showed that it yielded the most physically meaningful results. As discussed below, the results for the other boundary conditions, *8a* and *8b*, contain non-physical kinks in the solution near the entrance and exit boundaries, respectively, even when many grid points were assigned to those regions.

After discussing the steady-state results, dynamic calculations corresponding to boundary condition *8c* are presented.

Steady-State Results of Pearson-Petrie Model

Effect of Inflation Pressure

Figure 2 shows the bubble-tube radius corresponding to various values of inflation pressure ΔP when the outflow boundary condition (*Eq 8c*) is used. The radius increases with Z for inflation pressure ΔP = 250 and 270 Pa and decreases with Z for ΔP = 0 and 150 Pa. The radius profiles flatten out for Z > 10 cm because of the large increase in viscosity associated with decreasing temperature and increasing crystallinity. The blowup ratio (final radius/initial radius) increases with inflation pressure ΔP as expected. For an inflation pressure ΔP slightly above 270 Pa, the bubble becomes unstable and the bubble-tube radius approaches infinity, simulating a burst bubble.

Figure 3 gives the film thickness for the conditions corresponding to *Fig. 2*. The stretching force caused by increasing inflation pressure ΔP causes decreased film thickness H. At steady state, film velocity at each axial position Z is given by mass continuity as $V = V_0H_0R_0/HR$, assuming constant density. During transition to steady state, the relationship among V, R, and H is more complicated.

Figure 4 reports the blowup ratio (r at $\varsigma = L/R_0$) and thickness reduction (1/h) for the stable steady-state solutions computed for set values of B and F. For a fixed inflation pressure B, there is only one steady-state solution that intersects with the takeup ratio line ($v = 2.988$ at $\varsigma = L/R_0$). This implies that the

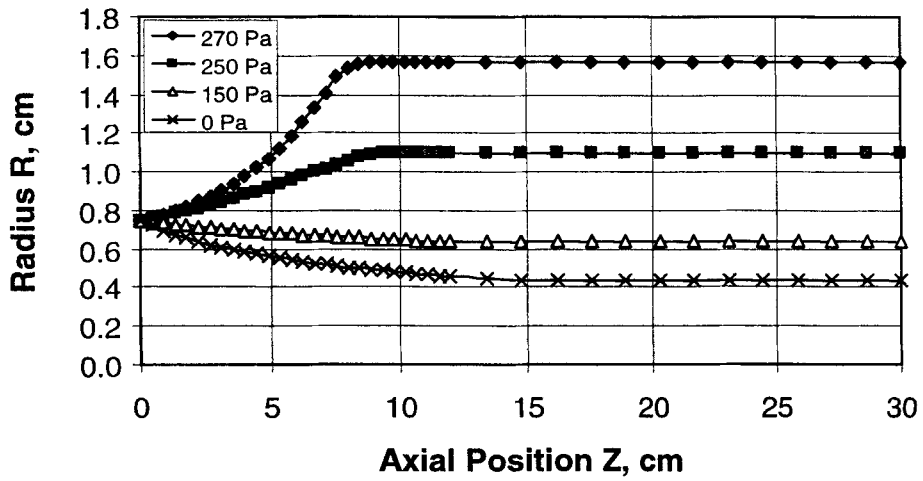

Fig. 2. Bubble-tube radius profiles vs. inflation pressure ΔP: steady-state, T_0 = 463 K, v_L = 2.988.

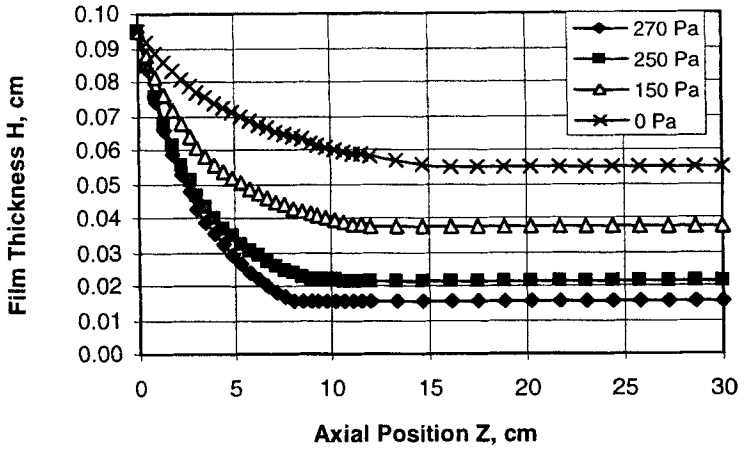

Fig. 3. Film thickness profiles vs. inflation pressure ΔP: steady-state, T_0 = 463 K, v_L = 2.988.

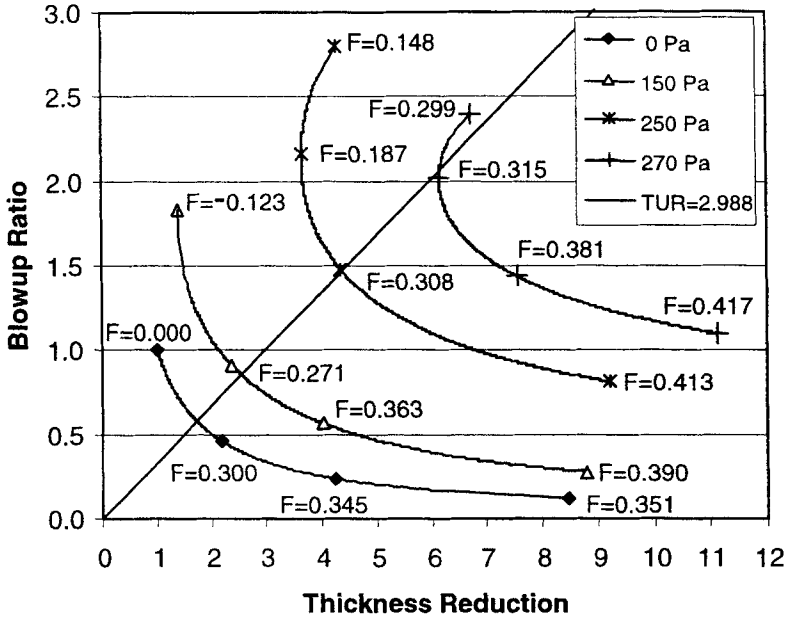

Fig. 4. Blowup ratio vs. thickness reduction for constant values of inflation pressure: steady-state, T_0 = 463 K.

blowup ratio increases monotonically with the inflation pressure. In generating the curves in *Fig. 4*, the modified tension F was progressively reduced from the value indicated on the lower right of each curve to the value indicated on the upper part of each curve. The modified tension F was a good continuation parameter for getting around the turning points in the curves corresponding to ΔP = 250 and 270 Pa.

The results shown in *Figs. 2* and *4* do not exhibit the nonintuitive qualitative behavior reported by Liu and coworkers (5, 20, 21) when attempting to simulate the steady-state Pearson-Petrie model. As the inflation pressure is increased, our results show an increase in blowup ratio rather than the decrease reported by Liu and coworkers in their simulation paper (5). Unlike their simulation results, our results are in agreement with their experimental findings (6). Liu and others (5, 22) used a boundary condition at the die exit (y = 0 at ς = 0), a special case of *Eq 8a* (with y_0 = 0), which differs from the one we used, *Eq 8c*. This difference in boundary condition may be responsible for their contradictory simulation results.

For a given value of the inflation pressure ΔP, adding a small amount of viscoelasticity to the constitutive relation has the effect of shifting the blowup ratio versus thickness reduction curves upward and to the right. This favors higher blowup ratios and thinner films. From the work of previous investigators (8, 22, 23), viscoelasticity is expected to increase stability by the strain-hardening effect.

Figures 5 and *6* show the temperature and crystallinity profiles for the various values of the inflation pressure ΔP. For inflation pressures of 250 Pa and 270 Pa, the flattening of the temperature for intermediate axial position Z is due to crystallization, which releases heat. As indicated in *Eq 9*, the rate of temperature decrease with respect to axial position Z is smaller dimensionless film thickness h. As shown in *Fig. 6*, the lower temperatures result in more crystallization for higher values of inflation pressure ΔP. This is expected, as *Eq 14* indicates that the rate of crystallization becomes nonzero when the temperature drops below the melt temperature θ_m and increases as temperature continues to drop.

The effect of crystallization on bubble-tube stabilization is profound. At X = 0.44, film viscosity, represented by *Eq 23* and the parametric values in *Table 3*, is increased by seven orders of magnitude from that of the melt emerging from the die.

The axial gradient, $y = \partial R/\partial Z$, of the bubble-tube radius R is plotted in *Fig. 7* for various values of inflation pressure ΔP. For inflation pressure ΔP = 250 and 270 Pa, the axial gradient y increases after the film leaves the die, and then declines rapidly to zero when reaching the frost zone at Z > 8 cm. At inflation pressure ΔP = 189.8 Pa, the radius profile remains perfectly flat for all values of Z; i.e., the axial gradient y = 0 uniformly. For inflation pressure ΔP = 0 and 150 Pa, the axial gradient y is negative as the film leaves the die, that is, the bubble-tube contracts. As the axial position Z increases, the axial gradient y approaches zero. Some investigators have solved the steady-state equations for blown film extrusion by guessing the axial gradient y at the die exit (Z = 0) and using a shooting method to achieve some type of boundary condition at Z = L (5, 22). Others have started by assuming that the axial gradient y = 0 at Z = L, and using a shooting method to get the correct boundary conditions on the variables at Z = 0 (24, 25, 26). In our case, and that of Cain and Denn (8), discretizing the axial position Z from Z = 0 to Z = L and using finite difference approximations to spatial derivatives allows the direct satisfaction of any downstream boundary condition. As mentioned, the results reported here are for the downstream boundary condition on the axial gradient y represented by *Eq 8c*.

Effect of Machine Tension

To examine the effect of machine tension on steady-state results, we found that the use of the modified tension $F = F_m - Br_f^2$ was more revealing than using F_m. For a die exit temperature of 463 K and conditions given in *Table 3*, the modified tension F was varied from 0 to a finite value to determine the range of inflation pressures that yielded stable solutions. Corresponding to each value of F, there is a lower and upper inflation pressure that allows physical solutions. Above the maximum inflation pressure, the radius grows uncontrollably, indicating a burst bubble. As shown in *Fig. 8*, the minimum inflation pressure is zero from F = 0 to F = 0.3450, but rises rapidly to equal the maximum inflation pressure at F = 0.4377. In the range between F = 0.3450 and F = 0.4377, as ΔP approaches the minimum inflation pressure from above, the bubble radius collapses to an infinitesimal quantity, mimicking a vanishingly thin filament traveling

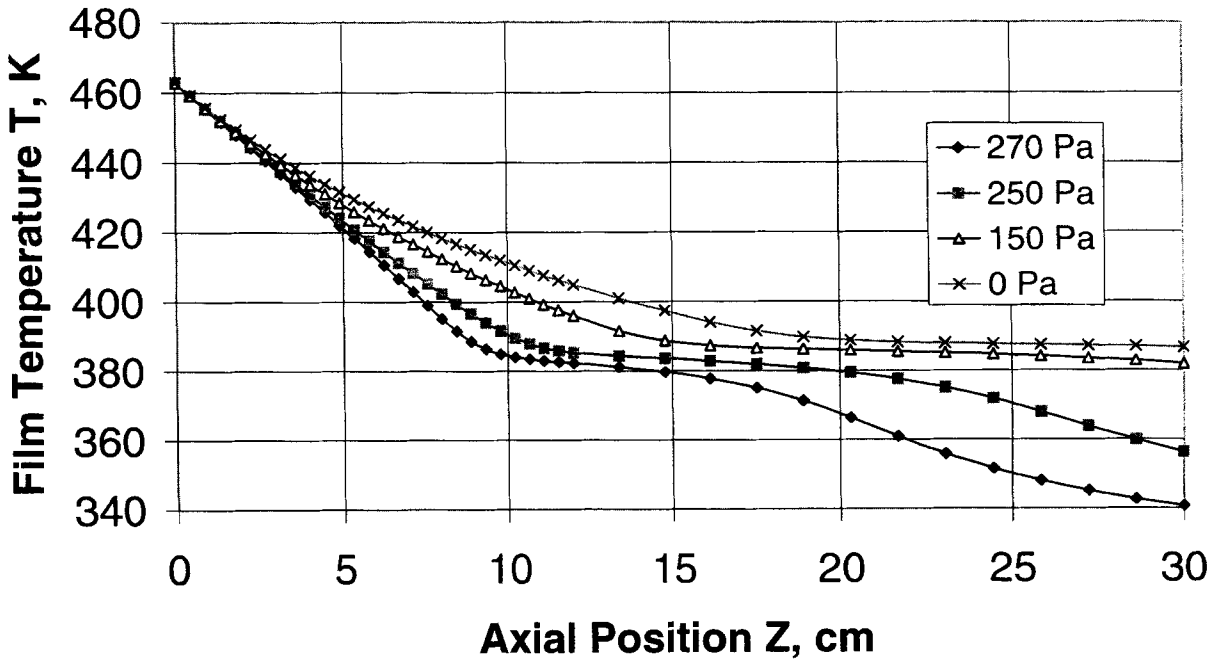

Fig. 5. Film temperature profiles vs. inflation pressure ΔP: steady-state, T_0 = 463 K, v_L = 2.988.

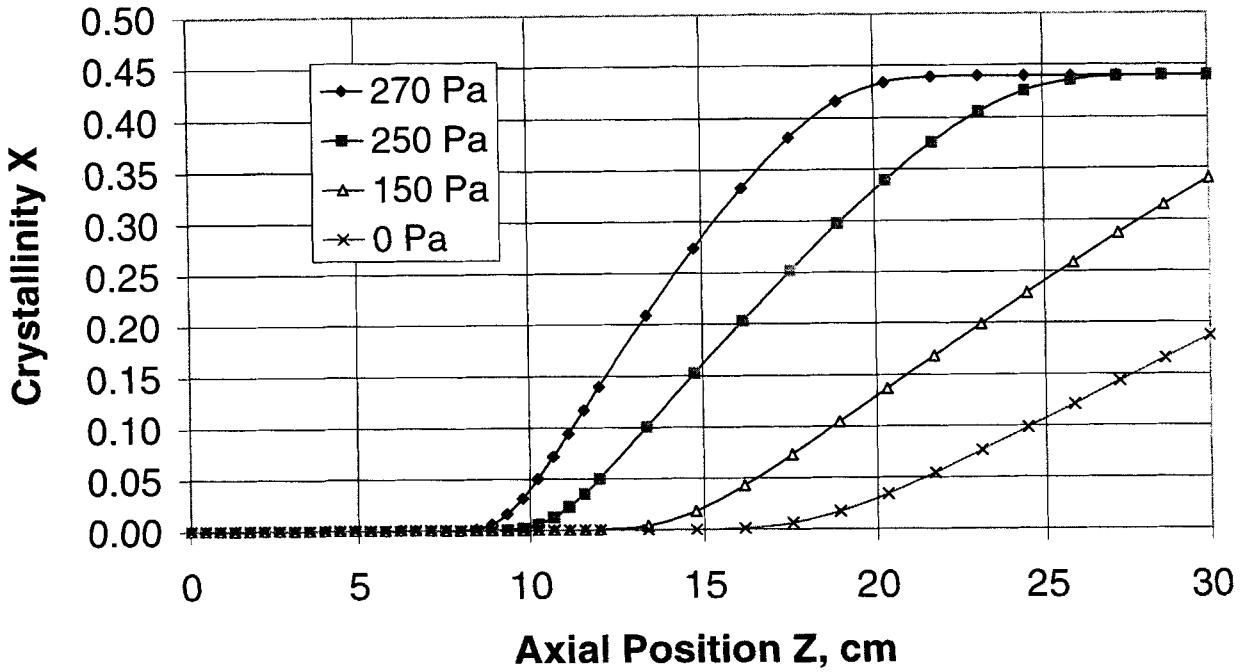

Fig. 6. Crystallinity profiles vs. inflation pressure ΔP: steady-state, T_0 = 463 K, v_L = 2.988.

at ever increasing speed. For F = 0 to 0.4377, there is no stable solution for inflation pressures either above the maximum or below the minimum. Above F = 0.4377, there is no stable solution for any inflation pressure.

In the negative range of the modified tension, F = 0 to −0.13, the maximum inflation pressure continues to decline, while the minimum inflation pressure rises above zero. Actually, a solution does exist below the minimum inflation pressure, but it corresponds to negative values of F_m, a non-operable condition. For F < −0.13, F_m is always negative.

Use of the modified tension F in *Fig. 8* instead of the tension F_m gave more revealing plots of the allowable

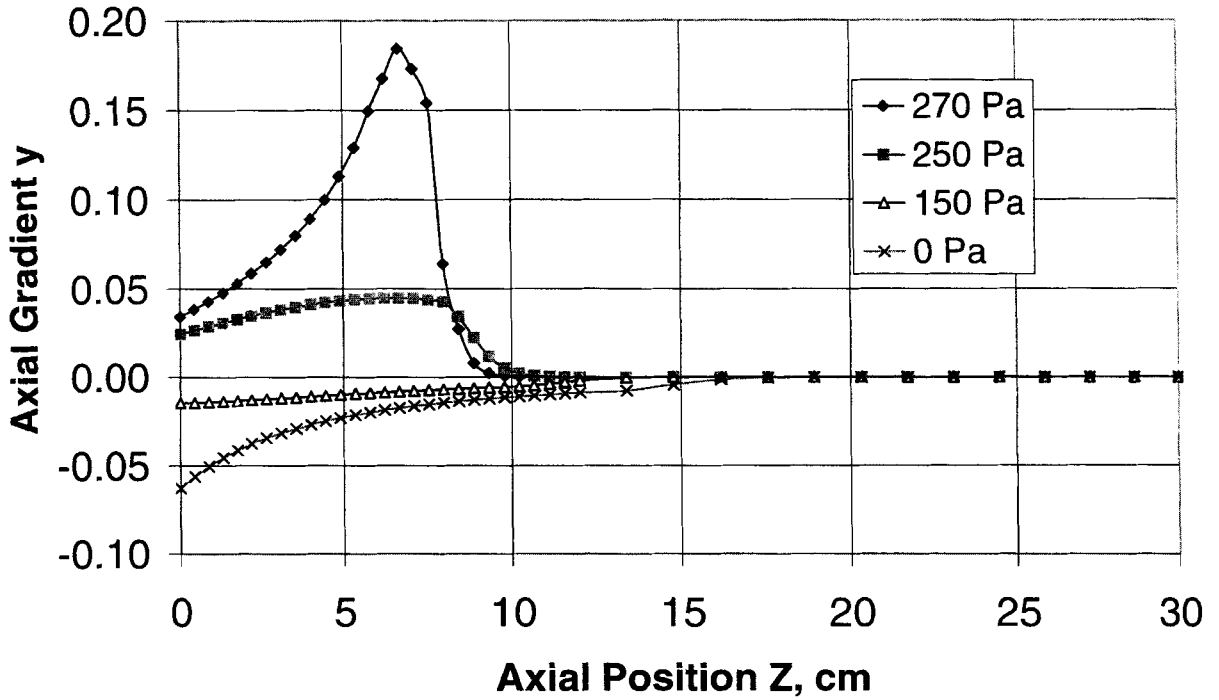

Fig. 7. Axial gradient profiles vs. inflation pressure ΔP: steady-state, T_0 = 463 K, v_L = 2.988.

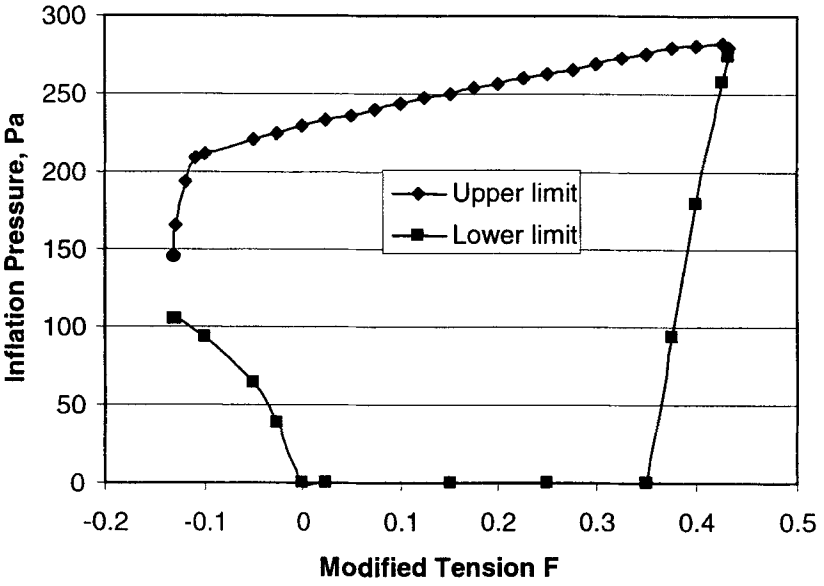

Fig. 8. Upper and lower inflation pressure bounds as a function of modified tension F.

ranges of inflation pressure ΔP (or B) as F varied monotonically while F_m sometimes exhibited nonmonotonic behavior.

Effect of Die Exit Temperature

To examine the effect of die exit temperature T_0 upon the process variables, the inflation pressure was set to ΔP = 250 Pa and the take-up ratio to v_L = 2.988. All other conditions being equal, the bubble radius is expected to grow larger as the die exit temperature T_0 is increased due to the reduction in viscosity. The radial profiles corresponding to die exit temperature T_0 = 443, 463, and 468 K are given in *Fig. 9*. The radius profiles increase with the die exit temperature T_0, which, unlike the computed results of Liu (20, 21), is physically reasonable.

Other Effects: Spatially Variable Inflation Pressure and Heat Transfer Coefficients

In order to make a one-on-one comparison with the calculations of Liu *et al.* (20, 21), the calculations just presented corresponded to spatially uniform inflation pressure and heat transfer coefficients. For completeness, however, we examined some other effects on the calculated steady-state results.

First, the heat transfer coefficient and the inflation pressure were varied spatially according to the calculated aerodynamic profiles of the external cooling air by Akaike *et al.* (9). These investigators used the k-ε method discussed by Abe *et al.* (27). Their calculations showed that the exterior surface pressure on the bubble-tube was negative near the die, followed by a rise to a positive value and then a decline to nearly zero. As a consequence, the inflation pressure ΔP corresponding to an inside bubble-tube pressure of 270 Pa gauge, had the profile shown in *Fig. 10*. In contrast, the heat transfer coefficient U_h calculated by Akaike *et al.* increased from a low value of approximately 10 W/(m²K) at the die to a higher value of approximately 190 W/(m²K) in the frost zone (about 7–10 cm) and then declined to a small value downstream of the frost zone (see *Fig. 11*). Sidiripoulos and Vlachapoulos (28) calculated similar behavior and attributed it to a combination of Coanda and Venturi effects.

Thus, the emerging melt near $\varsigma = 0$ would be subjected to a lower cooling rate and a higher inflation pressure than occurs in the case of constant U_h and ΔP. This combination of occurrences should threaten the stability of the bubble-tube at the entrance zone (near $\sigma = 0$) as it is subjected to greater stress while the viscosity of the melt is at its lowest value. In the case of the deformation thinning model in *Eq 23*, the bubble-tube burst at an extrusion temperature at T_0 = 463 K. A lower extrusion temperature, T_0 = 457.46 K, was required to keep the bubble-tube stable while achieving a similar blowup ratio. For a non-deformation-thinning model, e.g., one corresponding to $\lambda = 0$, the bubble-tube is less vulnerable to instability in the entrance zone near $\lambda = 0$, but the extrusion temperature T_0 must be higher, about 488 K.

Another spatial profile for U_h, based on the work of Kanai and White (29), was mentioned by Liu (20, 21). In this expression, U_h was held constant at $U_{h,0}$ from $Z = 0$ to $Z = Z_{crit}$, and then allowed to drop off as $U_{h,0}/Z^{2.5}$. Our calculations showed that this drop-off had very little effect on the results as long as Z was a few centimeters past the beginning of the frost zone. At this point, the film viscosity was several orders of magnitude higher than at $Z = 0$, and the geometric variables R and H were stabilized. As mentioned earlier,

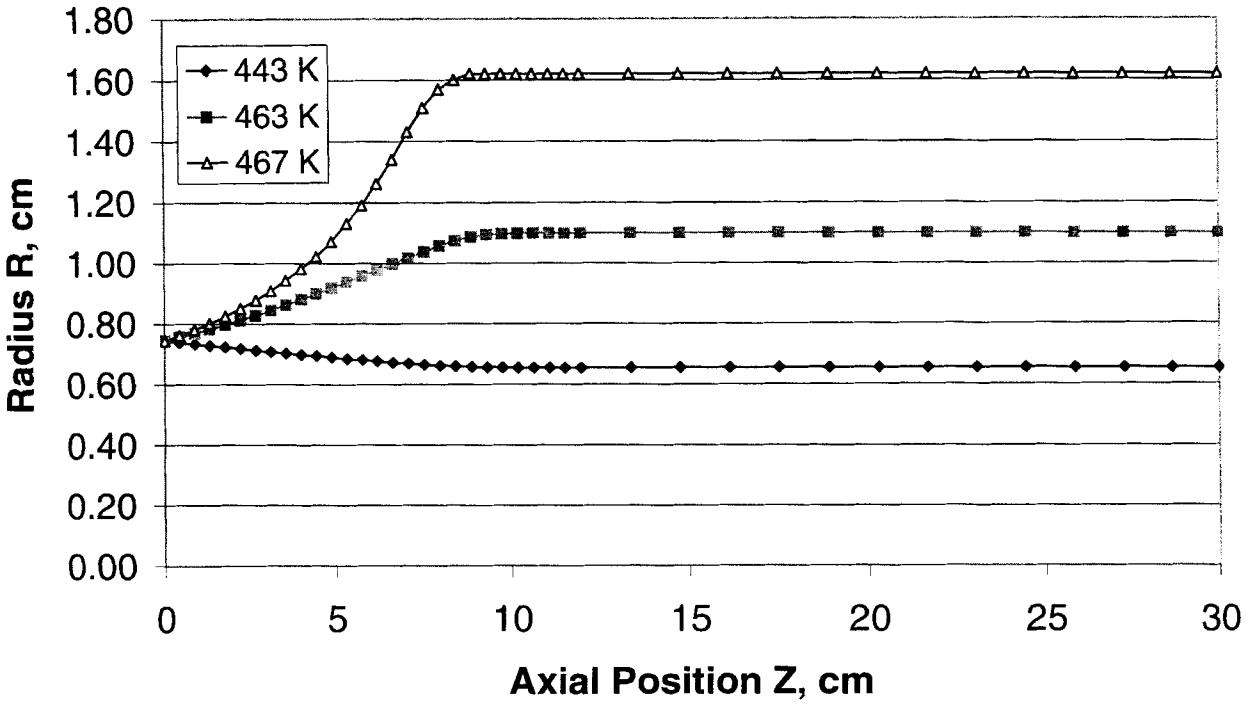

Fig. 9. Effect of die exit temperature T_0 upon bubble radius profiles.

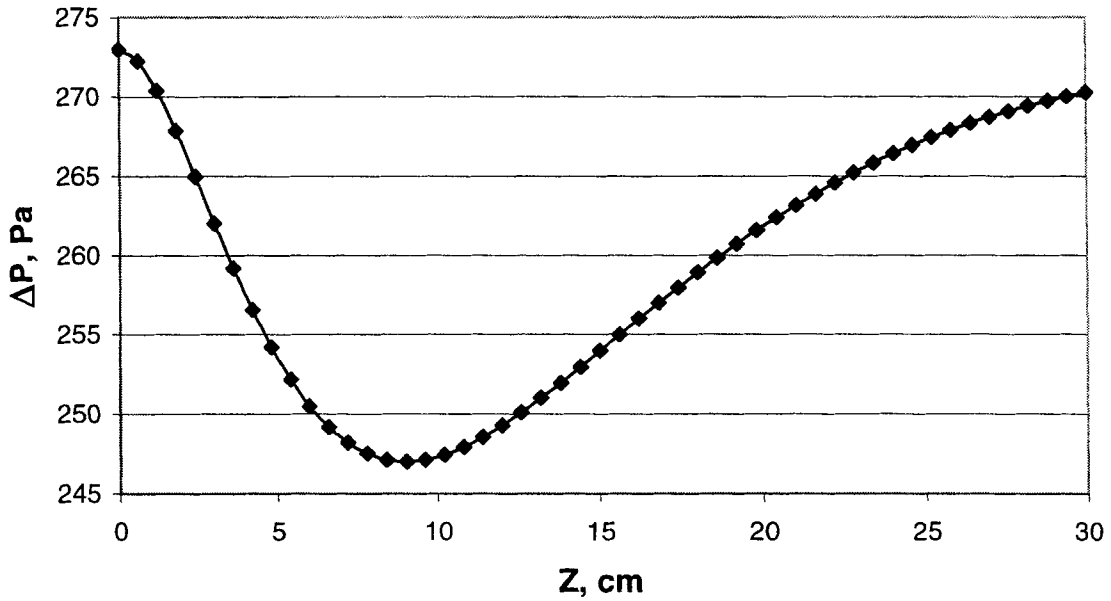

Fig. 10. Typical profile of inflation pressure resulting from aerodynamics of external cooling air; reference (9).

crystallization played a large role in the increase in viscosity, and a lack of crystallization would result in less film stability for the Kanai and White model.

Comparison of Boundary Conditions for the Axial Gradient y

There is some debate over the proper boundary condition for the axial gradient y of the bubble radius r. Here is a demonstration of why the outflow boundary condition 8c, which is called the "minimum order reduction" condition by Schiesser (30), was used. For the case of inflation pressure ΔP = 270 Pa and take-up ratio v_L = 2.988, *Fig. 12* compares steady-state profiles of the axial gradient y for boundary conditions *8a* and *8c*. The value of the axial gradient at the die, y_0, corresponding to boundary condition *8a* is taken

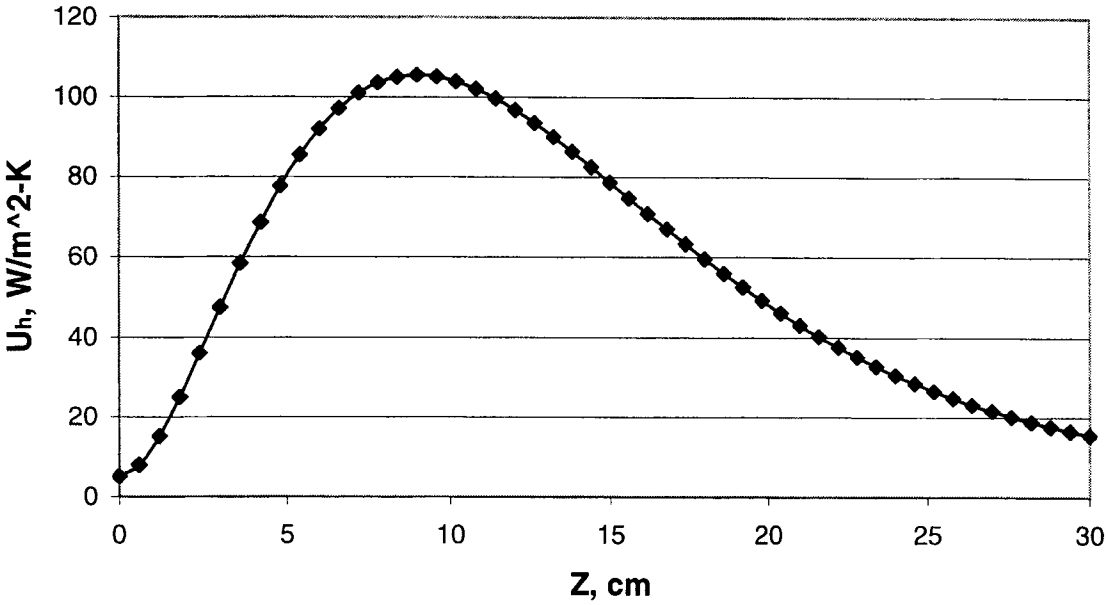

Fig. 11. Typical profile of heat transfer coefficient resulting from aerodynamics of external cooling air; reference (9).

to be zero. The boundary condition *8a* yields a nonphysical kink in the value of the axial gradient at the die exit, as it suddenly rises to attain nearly the same values as the plot for *Eq 8c*. If the correct value of the axial gradient $y = y_0$ at the die exit was known, then the boundary condition *8a* could be used without a kink occurring in the entrance zone of the solution. But, of course, the value for y_0 is not known in advance.

In *Fig. 13*, profiles for the bubble-tube radius R obtained using the different boundary conditions *8b* and *8c* are compared. There is a severe nonphysical wiggle at $Z = L$ when boundary condition *8b* is used. Such nonphysical wiggles due to this form of exit boundary condition are described in some detail by Schiesser (30). Refining the grid points did not eliminate this wiggle. For this reason, the outflow boundary condition *8c* was used.

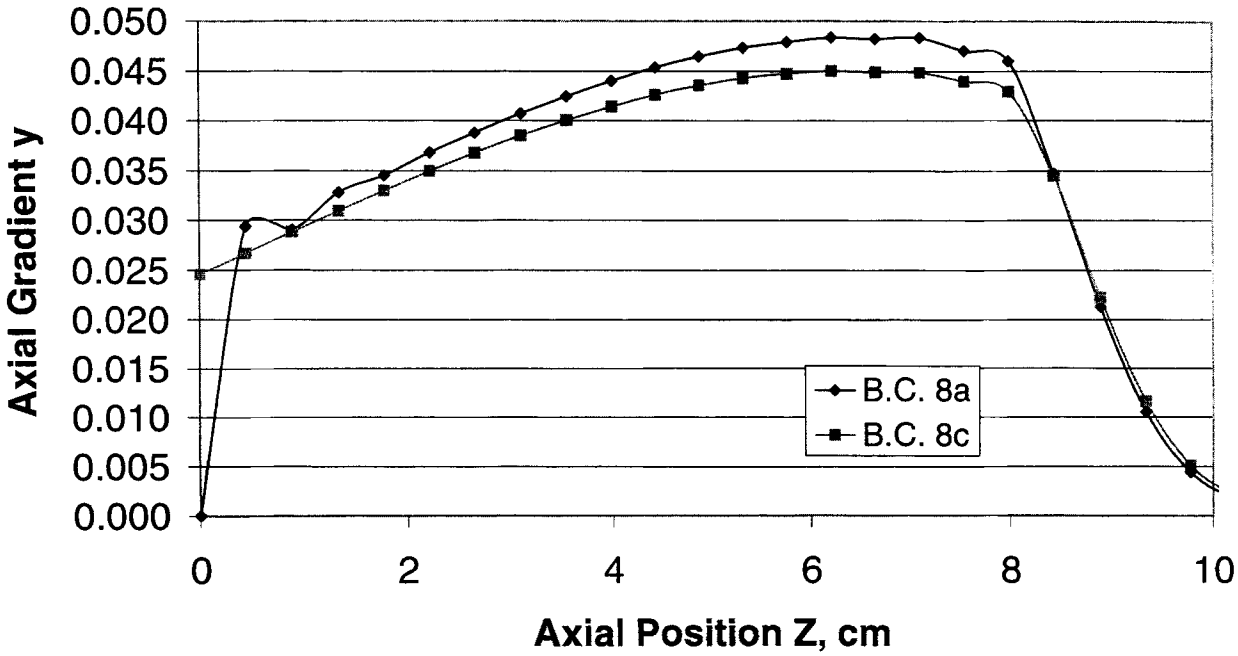

Fig. 12. Comparison of axial gradient profiles obtained from boundary conditions 8a and 8c.

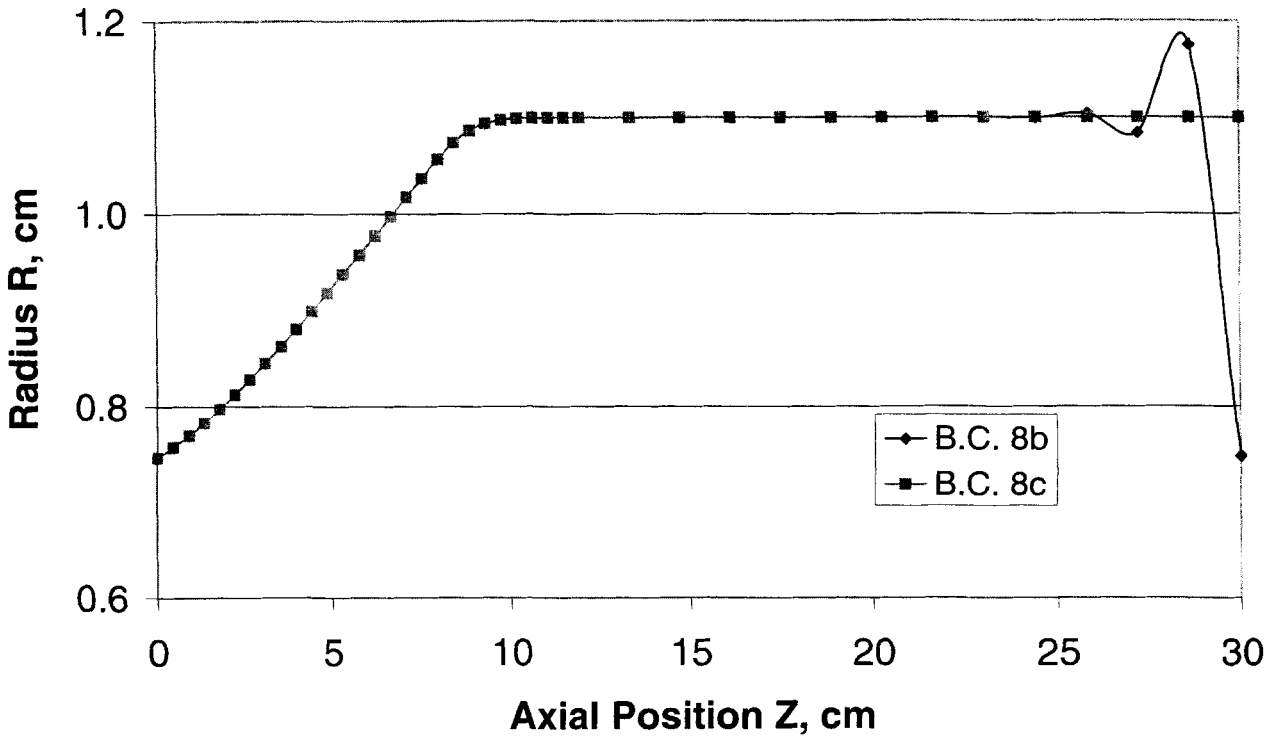

Fig. 13. Comparison of bubble-tube radius profiles obtained from boundary conditions 8b and 8c.

Dynamic Behavior of Pearson-Petrie Model

Several investigators have studied the dynamics of the Pearson-Petrie model by linearizing the nonlinear equations and computing the eigenvalues (8, 10, 14, 31). Here the transient nonlinear equations are solved to observe the evolution of process variables from startup to steady state. Specifically, we examine the effect that the shifting time has on the transition of process variables from one steady state to another. Also, the sensitivity of process variables to oscillations in the operating conditions is observed. In particular, the effects of variations of heat transfer coefficients, the inflation pressure ΔP, and the machine tension F upon the process operations are investigated.

Transient Shift Between Steady States

Of practical interest is how smoothly the blown film extrusion process can be shifted from one steady state to another. For the simulations here, the die exit temperature T_0 = 463 K, the take-up ratio v_L = 2.988, and the rest of the conditions are given in *Table 3*. The initial dimensionless inflation pressure B = 0.0654080 (this corresponds to ΔP = 125 Pa) and the modified tension F = 0.28376298. After the initial steady state is reached, the inflation pressure and machine tension are shifted to new values of B = 0.1308200 (this corresponds to ΔP = 250 Pa) and F = 0.31031428, respectively. In the simulation, the mathematical function used for the shift was

$$B_{new} = B_{old} + (B_{new} - B_{old})[1 - \exp(-\tau^2/\tau^2_{shift})] \quad (27)$$

$$F_{new} = F_{old} + (F_{new} - F_{old})[1 - \exp(-\tau^2/\tau^2_{shift})] \quad (28)$$

Because disturbances are rapidly propagated by the momentum balance (*Eq 2*) in the axial direction, the take-up ratio does not remain at 2.988 during this transition. Rather, the take-up ratio will experience a transitory departure in its steady-state value. The nature of this departure depends on the value of τ_{shift}, the shifting time, as indicated in *Fig. 14*. The longer the shifting time, the less the excursion of the take-up ratio v_L, and the smoother the transition. At a shifting time of 30, which is roughly the travel time of the film from Z = 0 to Z = L, the spike in v_L is greatly reduced. For below 20, the velocity profile overshoots and then sometimes undershoots its steady-state value. The major concern from the perspective of process operation is that this gyration in film velocity will cause wrinkling of the sheet unless the transition between steady states is made sufficiently gradual.

Figures 15–20 show how the dimensions and properties of the polymer bubble develop with respect to time using a shifting time τ_{shift} = 30. All of the profiles in *Figs. 15–20* develop smoothly with time, nearly reaching steady state in about 300 seconds (about 10 times L/V_0). *Figure 15* shows that bubble-tube radius at low axial positions responds more quickly than at the highest axial position (Z = L). This is to be expected, since changes in the polymer film take time to

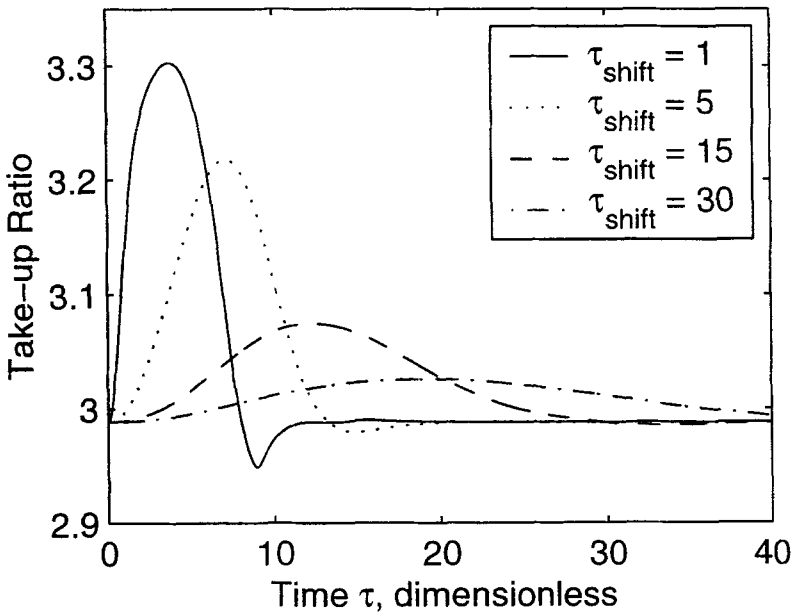

Fig. 14. Take-up ratio V_L after a shift in modified tension and inflation pressure.

propagate to the higher axial positions. A similar effect is seen in the film thickness (see *Fig. 16*) and temperature profiles (see *Fig. 18*). Also, the crystallinity profile climbs to its new steady-state value, reaching the maximum allowed value (X = 0.44) at Z = L (see *Fig. 19*). This dynamic effect is related to the constant value of crystallinity for Z = L achieved for a range of inflation pressure (see *Fig. 6*). Likewise, the axial gradient y of the bubble-tube radius progressively increases to its new steady-state profile (see *Fig. 20*). Similar behavior was observed for other values of the inflation pressure, die exit temperature, and take-up ratio.

Oscillations in Operating Conditions

Heat transfer from film to cooling air. In many experimental and smaller commercial blown film extruders, externally and internally flowing air streams cool the polymer film as it leaves the die. Proper cooling is important to get an acceptable viscosity profile and to obtain proper crystallization. The rate of cooling affects the dimensions (bubble-tube radius and film thickness) and strength of the bubble tube. The coefficient for film to air heat transfer U_h depends on the physical properties of the air as well as the pattern of flow in the boundary layer next to the film. In the calculations that follow, the inflation pressure ΔP = 265 Pa, the time-averaged take-up ratio v_L = 2.988, and the die exit temperature T_0 = 463 K. The other conditions and physical properties are given in *Table 3*.

The heat transfer coefficient was assumed to be a sinusoid with frequency ν and amplitude of either 2% or 4% of the steady value (the bubble was unstable for constant values of the heat transfer coefficient above 4% of the nominal value). The maximum positive and negative deviations of the final bubble-tube radius

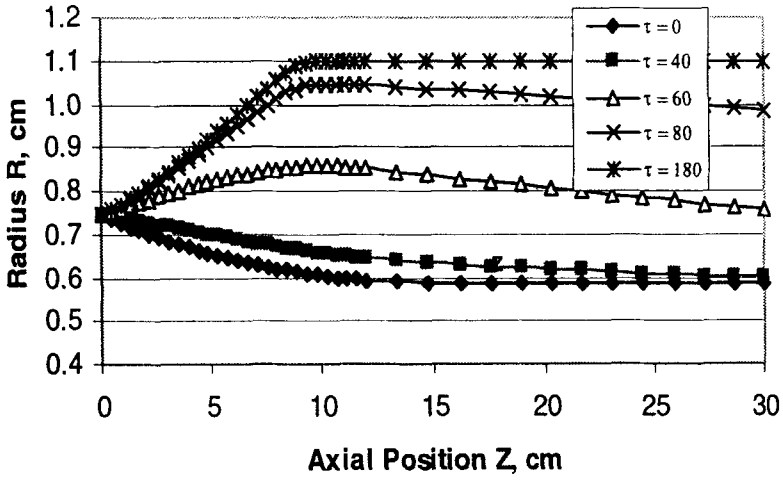

Fig. 15. Bubble-tube radius profiles after shift to new inflation pressure ΔP and modified tension F (τ_{shift} = 30).

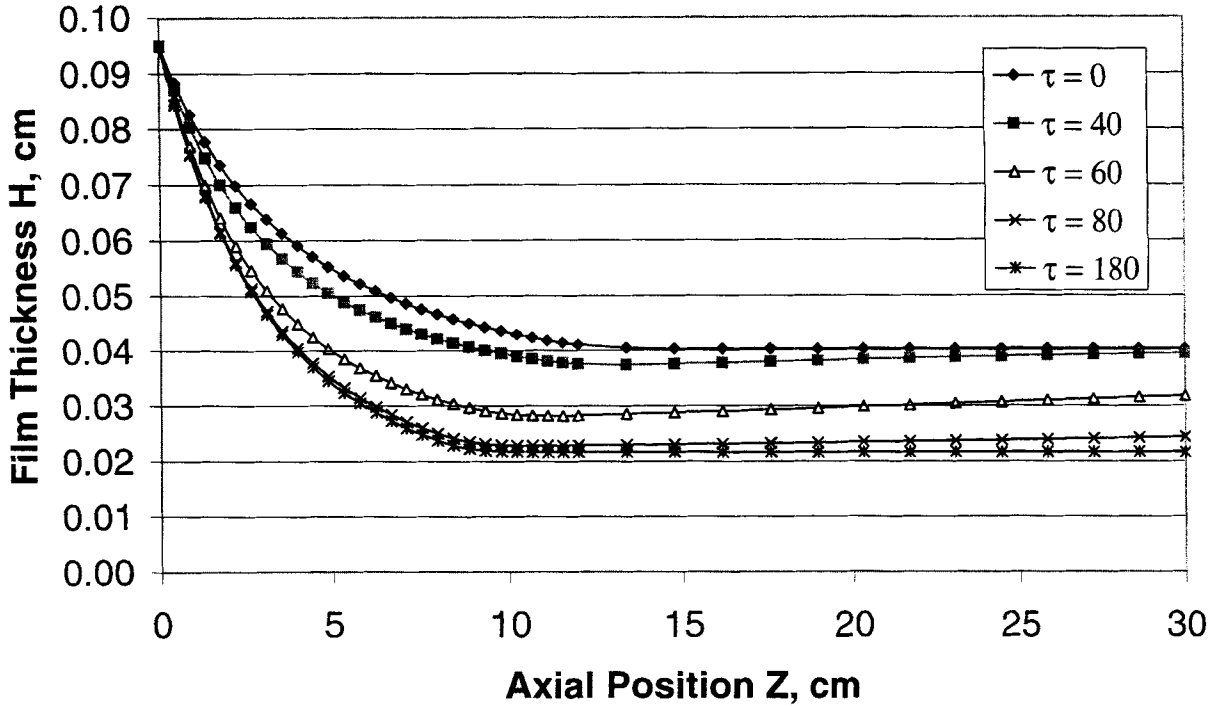

Fig. 16. Film thickness profiles after shift to new inflation pressure ΔP and machine tension F (τ_{shift} = 30).

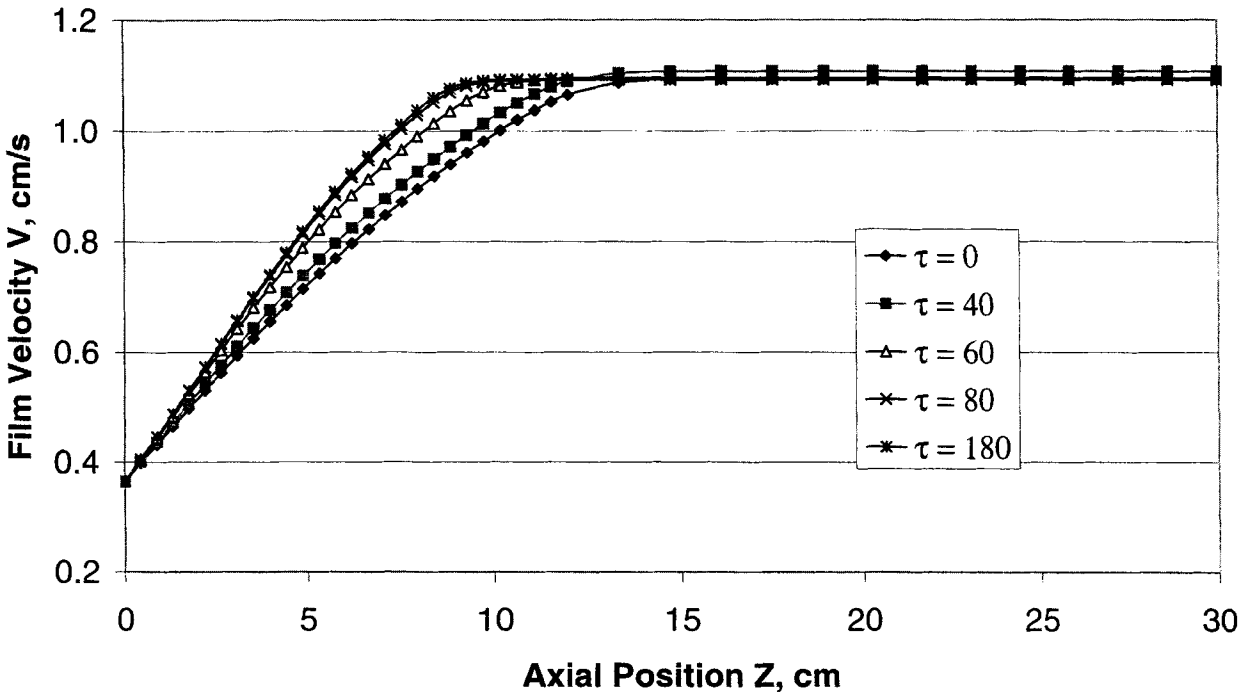

Fig. 17. Film velocity profiles after shift to new inflation pressure ΔP and modified tension F (τ_{shift} = 30).

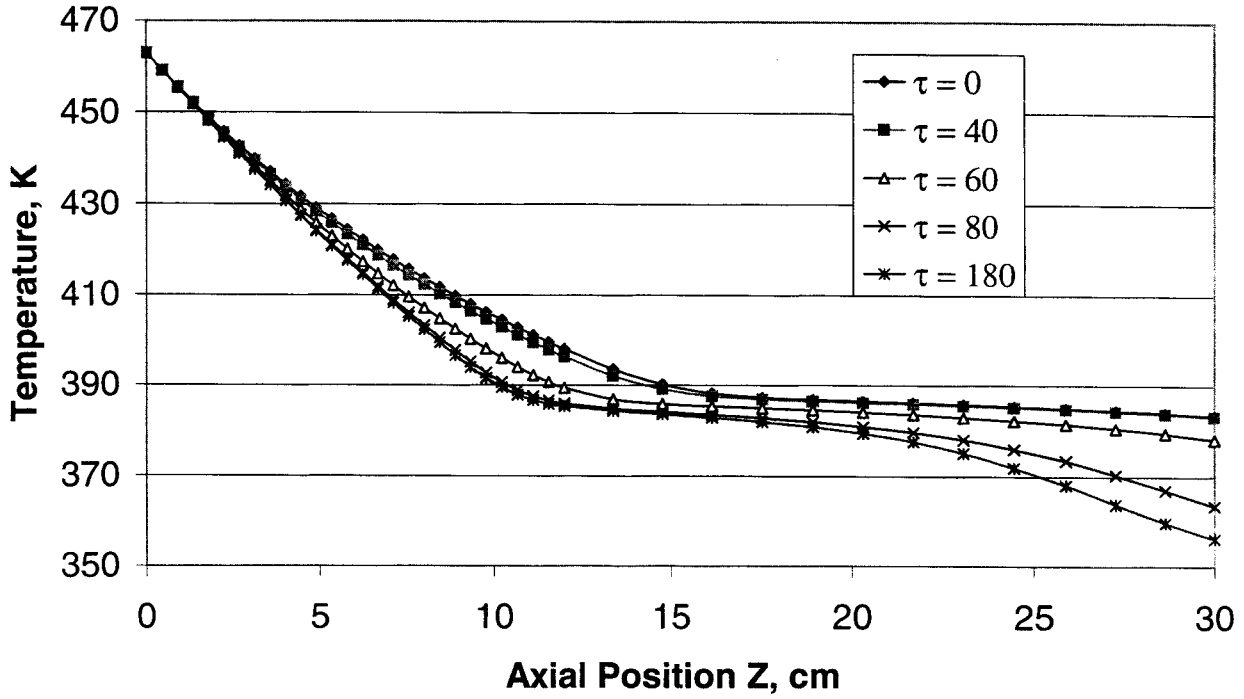

Fig. 18. Film temperature profiles after shift to new inflation pressure ΔP and machine tension F (τ_{shift} = 30).

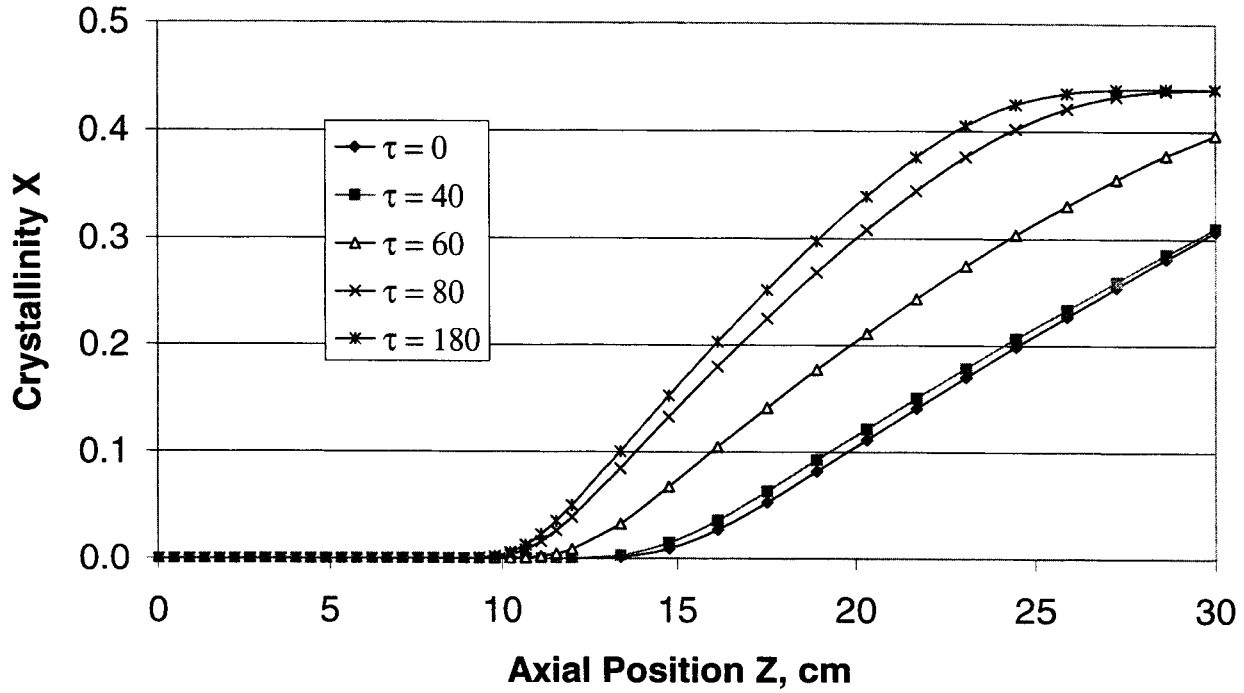

Fig. 19. Crystallinity profiles after shift to new inflation pressure ΔP and modified tension F (τ_{shift} = 30).

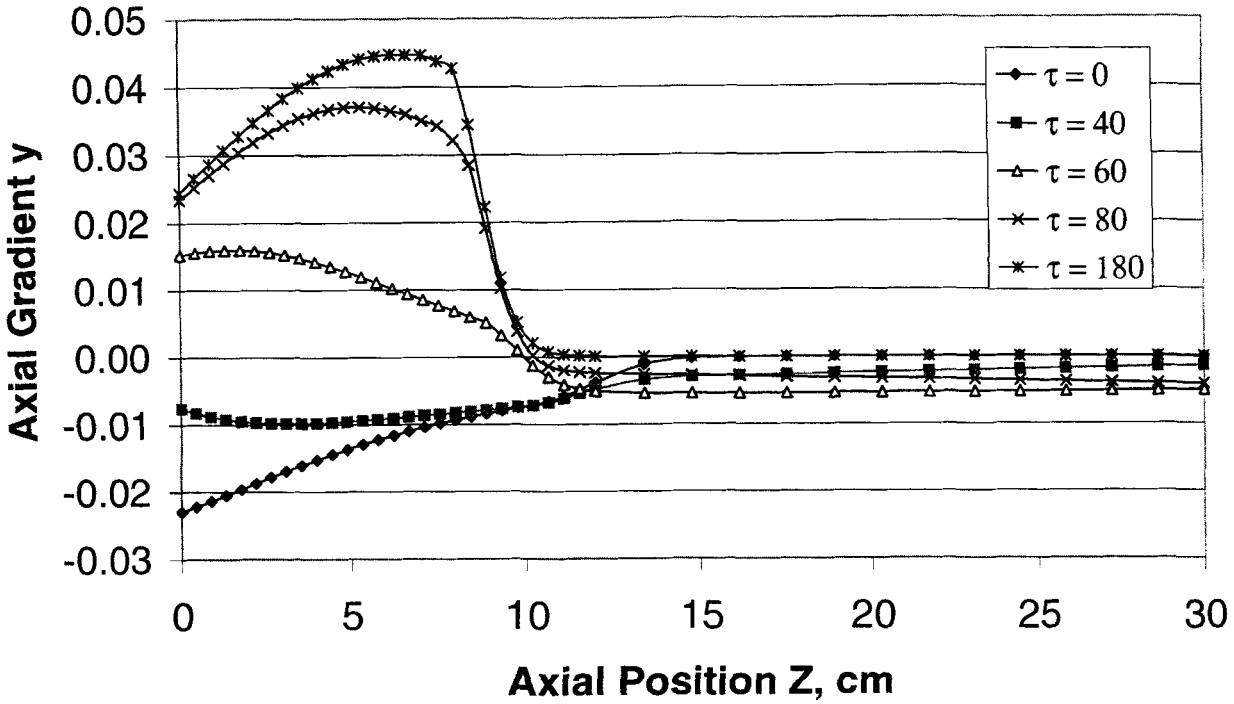

Fig. 20. Axial gradient of bubble-tube radius profiles after shift to new inflation pressure ΔP and modified tension F (τ_{shift} = 30).

(that is, the radius r_L at the top of the freeze zone) as a function of frequency of oscillation are shown in *Fig. 21*. The frequency of variation of r_L follows the frequency in the oscillation of the heat transfer coefficient U_h extremely closely and is practically equal to ν. The positive and negative deviations, $r_L - r_{L,ss}$, are not symmetric about zero. This lack of symmetry can be attributed to the nonlinearity of the system with respect to the temperature effect on the viscosity. As expected for a physical system, the maximum deviation declines rapidly at higher frequencies.

The mean variation $r_{L,m}$ (upper value minus lower value of $r_L - r_{L,ss}$ divided by two) is plotted versus frequency ν in *Fig. 22* for amplitudes of oscillation in heat transfer coefficient U_h of 2% and 4%. The maximum mean variation in $r_{L,m}$ (for low values of ν_h) is sensitive to variation in the heat transfer coefficient U_h. At low frequencies, changes of 2% and 4% in the heat transfer coefficient U_h correspond to changes in the bubble-tube radius r_L of 6.4% and 17.4%, respectively. The maximum mean variation is more than two orders-of-magnitude smaller for frequencies higher than 0.32.

There is a kink in the plots around the frequency 0.2. The kink persisted when the calculations were repeated for increasing number of grid points, suggesting that the kink is a real characteristic of the dynamic relationship between heat transfer coefficient variations and the bubble-tube radius. This kink suggests a partial separation of time scales in the dynamic behavior of the process. These time scales are not easily attributed to single groups of governing equations because of their coupling.

Inflation air pressure. Here is a determination of the effect of oscillations of the inflation pressure on the operation of blown film extrusion. The base inflation pressure is 265 Pa, the machine tension F is held at 0.311, and the amplitude of oscillation is taken be either 1.2% or 2.4%. For constant values of machine tension above 2.4%, the bubble was unstable and burst. For a 2.4% variation of inflation pressure about the inflation pressure ΔP = 265 Pa, *Fig. 23* shows the maximum positive and negative deviations in the final bubble-tube radius r_L as a function of frequency ν. The deviations are not symmetrical about zero (and hence the dynamic behavior is significantly nonlinear), and the deviations do not decrease monotonically with frequency. At the frequency ν = 0.12, the deviations reach a local minimum in magnitude, then climb to a local maximum at ν = 0.15 before resuming a decrease toward zero. At low frequencies, small changes in the inflation pressure ΔP cause large changes in the bubble-tube radius r_L, with 1.2% and 2.4% variations in ΔP resulting in 7.8% and 25.2% maximum variation, respectively, in r_L.

The mean deviation in the bubble-tube radius r_L (upper value minus lower value of $r_L - r_{L,ss}$ divided by two) is plotted as a function of frequency ν in *Fig. 24* for 1% and 2% amplitude in variations of inflation pressure ΔP about 265 Pa. Here the local minimum and maximum are more evident in the region ν = 0.12 to 0.15. The maximum mean variation is more than two orders-of-magnitude smaller for frequencies higher than 0.1 than for low frequencies.

Machine tension. Here is an investigation of the effect of oscillating machine tension on the behavior of

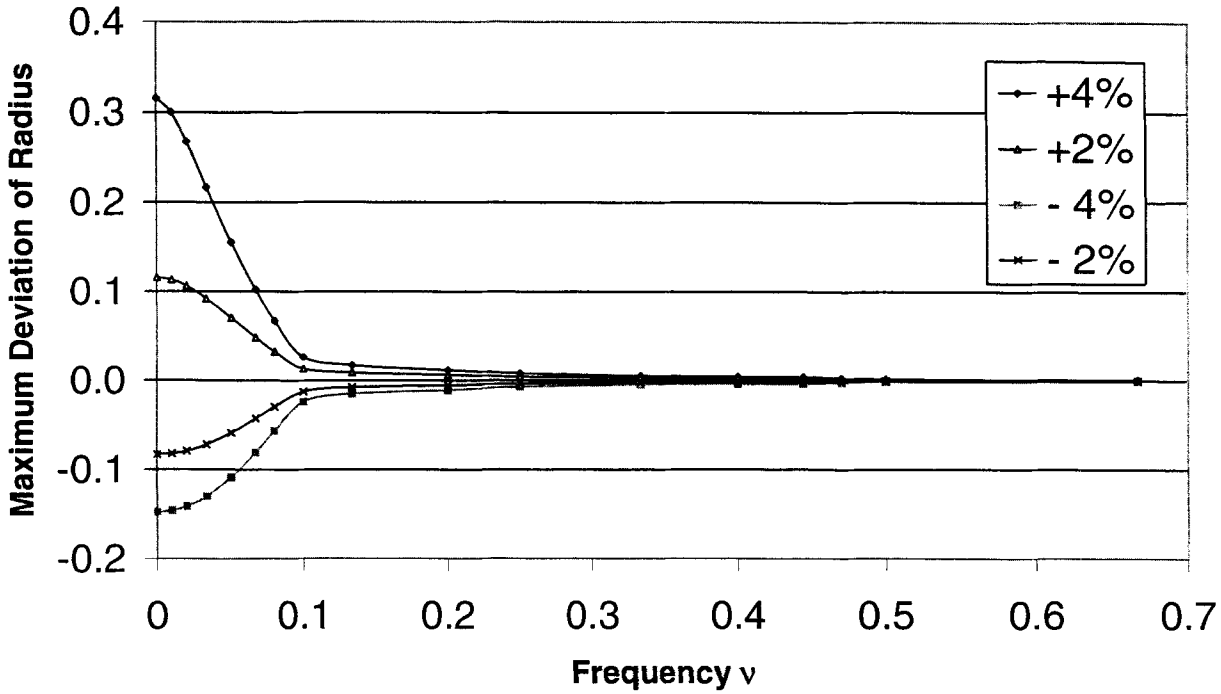

Fig. 21. Maximum deviation of final bubble radius as a function of the frequency of oscillation of the heat transfer coefficient U_h.

the blown film extrusion process. The base value of the modified tension F is taken as 0.311, and the amplitude of oscillation is taken as 11.5% around this value. The maximum deviations of the bubble-tube radius r_L as a function of the frequency of oscillation are shown in *Fig. 25*. Unlike the cases involving heat transfer or inflation pressure, the upper and lower values of the maximum deviation are relatively symmetrical with respect to zero, which occurs for linear relationships between variables. The maximum deviations in the bubble-tube radius are similar in magnitude for oscillations in inflation pressure and machine

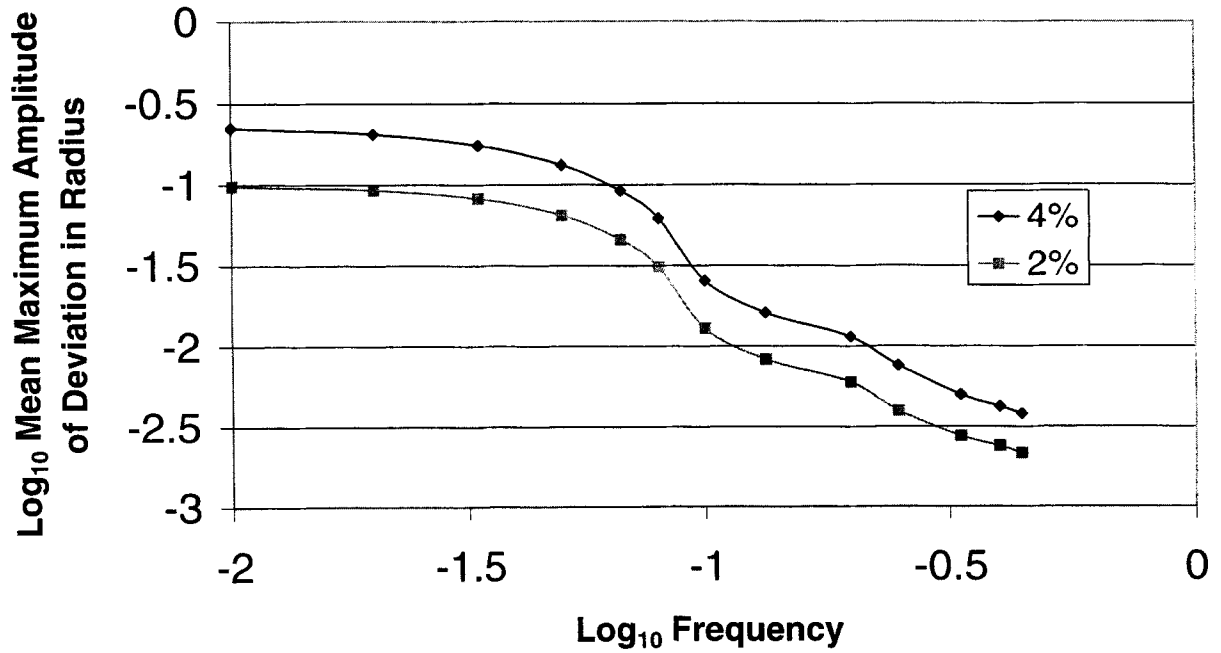

Fig. 22. Mean maximum amplitude of deviation in the final bubble radius r_L resulting from 2% and 4% variation in the heat transfer coefficient U_h.

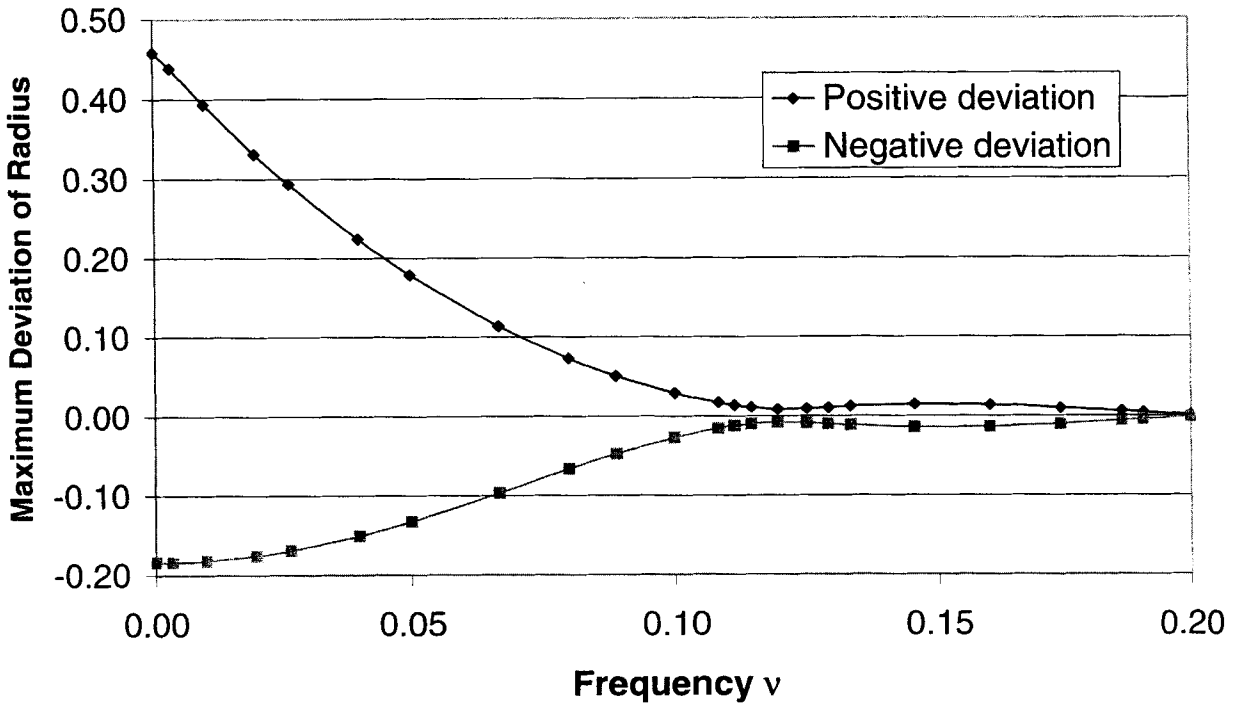

Fig. 23. Maximum deviation of the final bubble radius r_L as a function of the frequency of oscillation of inflation pressure ΔP.

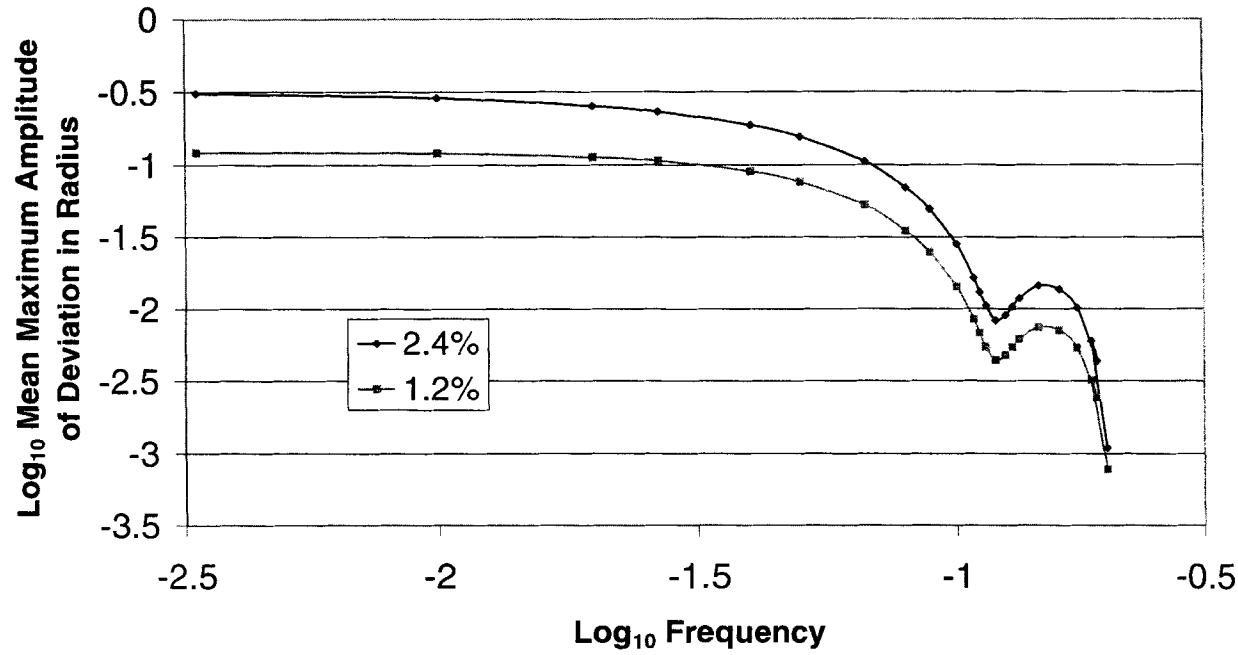

Fig. 24. Mean maximum amplitude of deviation of final bubble radius r_L resulting from oscillation of the inflation pressure ΔP.

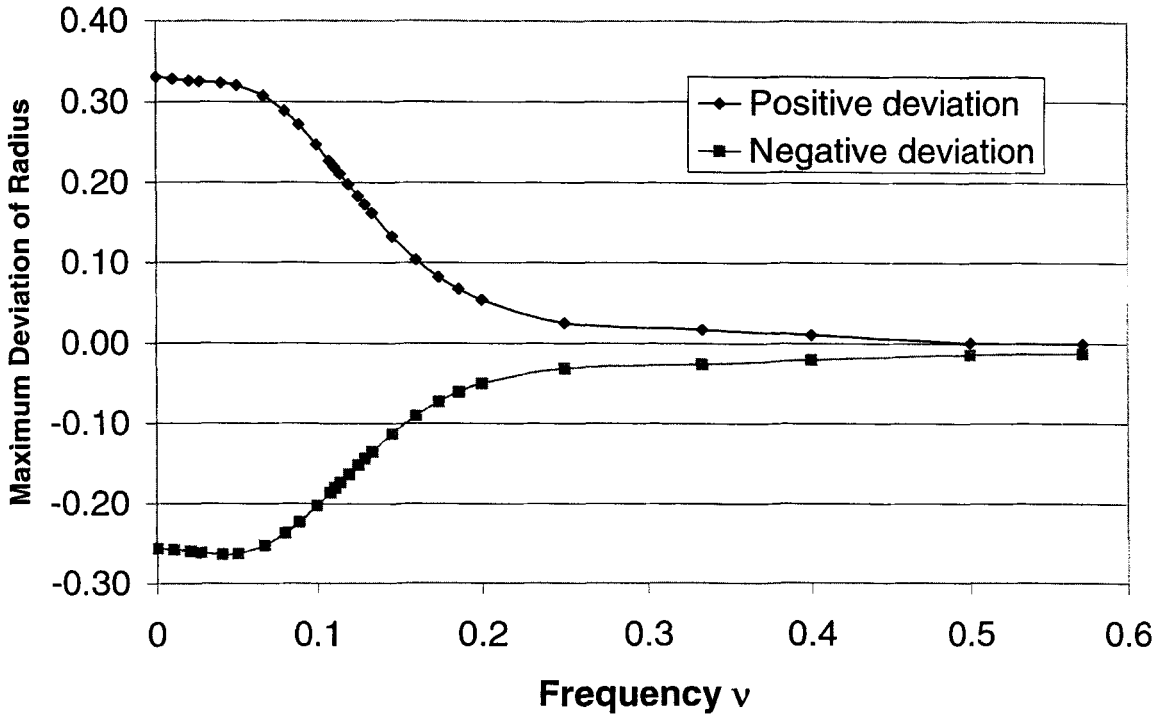

Fig. 25. Maximum deviation of the final bubble radius r_L as a function of the frequency of oscillation of the modified tension F (11.5% amplitude).

tension (compare *Figs. 23* and *25*), although the relative maximum change in machine tension was much greater than the maximum change in inflation pressure (2%). This indicates that the bubble-tube radius is much more sensitive to oscillations in the inflation pressure than oscillations in machine tension.

In *Fig. 26*, the mean maximum deviation in r_L is plotted as a function of frequency ν for the 11.5% amplitude in oscillation of the modified tension F. The roll-off of the amplitude is much more gradual as a function of frequency than for the heat transfer coefficient and inflation pressure, indicating that high

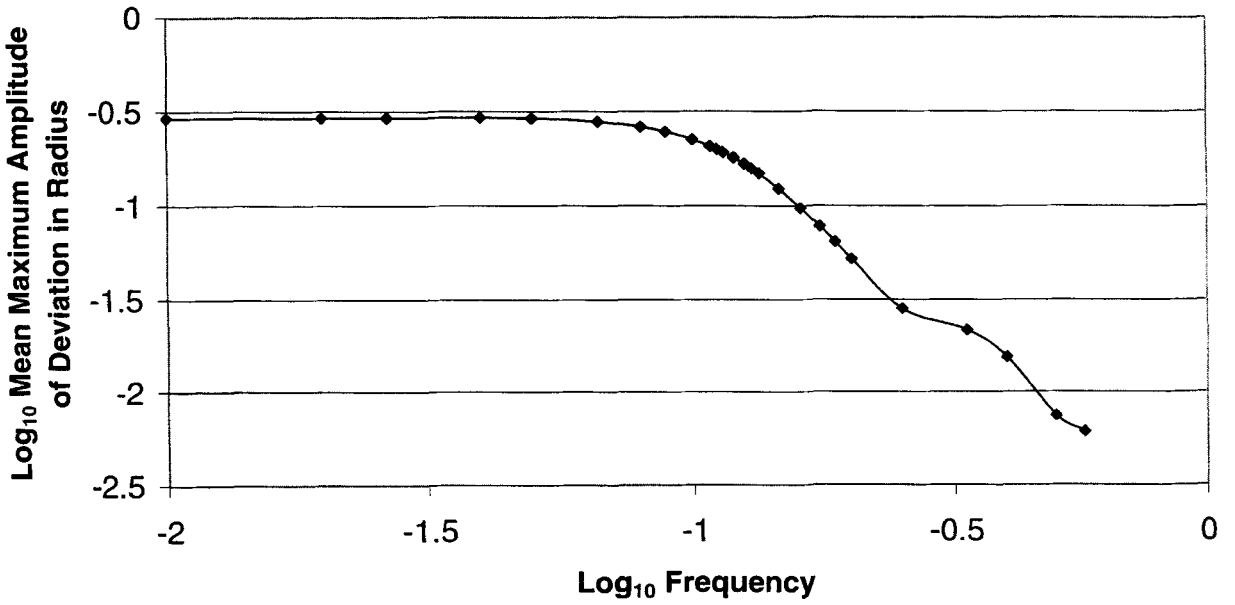

Fig. 26. Mean maximum amplitude of deviation of final bubble radius r_L resulting from oscillation of the modified tension F (11.5% amplitude).

frequency oscillations in the machine tension have a stronger relative effect. This result agrees with physical intuition, since high frequency oscillations in machine tension rather directly affect the bubble geometry, whereas the effect of high frequency oscillations in heat transfer coefficient and inflation pressure receive more damping by the thermal and physical inertia of the polymer film. The maximum mean variation is one order-of-magnitude smaller for a frequency of 0.27 than for low frequencies.

CONCLUSIONS

When the NMOL approach is used to solve the two-point boundary value problem that comprises the Pearson-Petrie thin film blown film extrusion model, the results are in good qualitative agreement with experiment. The bubble-tube radius is seen to increase with inflation pressure under a wide range of conditions. This suggests that the "counterintuitive" simulation results of Liu and coworkers (5, 20, 21) and Ashok and Campbell (22) resulted from application of an incorrect boundary condition (*Eq 8a*) or numerical inaccuracies exacerbated by not knowing the true value of the axial gradient y at the die exit. The boundary conditions and numerical method used here avoid such problems.

When the blown film process is started up, undergoes a deliberate change, or suffers an upset, the dynamic model can be easily solved to predict the outcome. The dynamic model readily reveals the effect of oscillations in operating conditions such as heat transfer, inflation pressure, or machine tension on film bubble-tube dynamics. The dynamic model can be used to quantify the extent of nonlinearity between relevant process variables, or to design process control systems.

ACKNOWLEDGMENTS

The authors thank Mitsuko Fujiwara for help in manuscript preparation, and the National Center for Supercomputing Applications and Procter and Gamble for support.

REFERENCES

1. S. Middleman, *Fundamental Studies of Polymer Processing*, McGraw-Hill, New York (1977).
2. W. E. Schiesser, *The Numerical Method of Lines Integration of Partial Differential Equations*, Academic Press, San Diego (1991).
3. J. R. A. Pearson and C. J. S. Petrie, *J. Fluid Mech.*, **40**, 1 (1970).
4. J. R. A. Pearson and C. J. S. Petrie, *J. Fluid Mech.*, **42**, 609 (1970).
5. C.-C. Liu, D. C. Bogue, and J. E. Spruiell, *Intern. Polym. Process.*, **10**, 230 (1995).
6. C.-C. Liu, D. C. Bogue, and J. E. Spruiell, *Intern. Polym. Process.*, **10**, 226 (1995).
7. A. K. Doufas and A. J. McHugh, *J. of Rheology*, **45**, 1085 (2001).
8. J. J. Cain and M. M. Denn, *Polym. Eng. Sci.*, **28**, 1527 (1988).
9. O. Akaike, T. Tsuiji, and Y. Nagano, *Intern. Polym. Process.*, **14**, 168 (1999).
10. K.-S. Yoon and C.-W. Park, *Intern. Polym. Process.*, **14**, 342 (1999).
11. C. J. S. Petrie, *AIChE J.*, **21**, 275 (1975).
12. K.-S. Yoon and C.-W. Park, *Polym. Eng. Sci.*, **32**, 1771 (1992).
13. S. M. Alaie and T. C. Papanastasiou, *Intern. Polym. Process.*, **8**, 51 (1993).
14. Y. L. Yeow, *J. Fluid Mech.*, **75**, 577 (1976).
15. R. A. Novy, H. T. Davis, and L. E. Scriven, *Chem. Eng. Sci.*, **46**, 57 (1991).
16. C. A. Silebi and W. E. Schiesser, *Dynamic Modeling of Transport Process Systems*, p. 409, Academic Press, San Diego (1992).
17. L. R. Petzold, "A description of DASSL: a differential/algebraic system solver," In R.S. Stepleman, ed., *Scientific Computing*, pp. 65–68, IMACS, North-Holland (1983).
18. T. Maly and L. R. Petzold, *Appl. Numer. Math.*, **20**, 57 (1996).
19. F. Scheid, Numerical Analysis, p. 311, McGraw-Hill, New York (1968).
20. C.-C. Liu, *Studies of Mathematical Modelling and Experimental On-Line Measurement Techniques for the Tubular Film Blowing Process*, M.S. thesis, Dept. of Materials Science and Engineering, University of Tennessee, Knoxville (1991).
21. C.-C. Liu, *On-Line Experimental Study and Theoretical Modelling of Tubular Film Blowing*, Ph.D. thesis, Dept. of Materials Science and Engineering, University of Tennessee, Knoxville (1994).
22. B. K. Ashok and G. A. Campbell, *Intern. Polym. Process.*, **7**, 240 (1992).
23. K.-S. Yoon and C.-W. Park, *J. Non-Newtonian Fluid Mech.*, **89**, 97 (2000).
24. X.-L. Luo and R. I. Tanner, *Polym. Eng. Sci.*, **25**, 620 (1985).
25. J. R. A. Pearson and C. J. S. Petrie, *Plast. Polym.*, **38**, 85 (1970).
26. T. Kanai and J. L. White, *J. Polym. Eng.*, **5**, 3277 (1975).
27. K. Abe, T. Kondoh, and Y. Nagano, *Int. J. Heat & Mass Transfer*, **38–8**, 1467 (1995).
28. V. Sidiropoulos and J. Vlachopoulos, *Polym. Eng. Sci.*, **40**, 1611 (2000).
29. T. Kanai and J. L. White, *Polym. Eng. Sci.*, **24**, 1185 (1984).
30. W. E. Schiesser, *Appl. Numer. Math.*, **20**, 171 (1996).
31. H. Andrianarahinjaka and P. Micheau, *Comptes Rendus de L'Academie des Sciences Series IIB-Mechanique, Physique, Chimie, Astronomie*, **322**, 363 (1996).